Geochemistry, Geophysics, Geosystems®

AGU ADVANCING EARTH AND SPACE SCIENCES

METHOD

10.1029/2023GC010872

Special Section:
Frontiers in lithospheric dynamics: bridging scales through observations, experiments, and computations

Numerical Modeling of Earthquake Cycles Based On Navier-Stokes Equations With Viscoelastic-Plasticity Rheology

Haibin Yang[1], Louis Moresi[2], Huihui Weng[3], and Julian Giordani[4]

[1]School of Earth Sciences, Zhejiang University, Hangzhou, China, [2]Research School of Earth Sciences, Australian National University, Canberra, ACT, Australia, [3]School of Earth Sciences and Engineering, Nanjing University, Nanjing, China, [4]School of Geosciences, Sydney University, Sydney, NSW, Australia

Key Points:

- We build code modeling earthquake cycles based on the long-term tectonic modeling software Underworld
- Benchmarks at the earthquake timescale are used to demonstrate the effectiveness of our approach
- Cratons may remain two peaks in surface uplift profiles near the active fault for >1000 years after one characteristic earthquake

Supporting Information:

Supporting Information may be found in the online version of this article.

Correspondence to:

H. Yang,
haibin.yang@zju.edu.cn

Citation:

Yang, H., Moresi, L., Weng, H., & Giordani, J. (2023). Numerical modeling of earthquake cycles based on Navier-Stokes equations with viscoelastic-plasticity rheology. *Geochemistry, Geophysics, Geosystems*, *24*, e2023GC010872. https://doi.org/10.1029/2023GC010872

Received 30 JAN 2023
Accepted 22 AUG 2023

Author Contributions:

Conceptualization: Haibin Yang
Formal analysis: Huihui Weng
Funding acquisition: Louis Moresi
Investigation: Haibin Yang, Huihui Weng, Julian Giordani

Abstract Visco-elastic-plastic modeling approaches for long-term tectonic deformation assume that co-seismic fault displacement can be integrated over 1000s–10,000s years (tens of earthquake cycles) with the appropriate failure law, and that short-timescale fluctuations in the stress field due to individual earthquakes have no effect on long-term behavior. Models of the earthquake rupture process generally assume that the tectonic (long-range) stress field or kinematic boundary conditions are steady over the course of multiple earthquake cycles. This study is aimed to fill the gap between long-term and short-term deformations by modeling earthquake cycles with the rate-and-state frictional (RSF) relationship in Navier-Stokes equations. We reproduce benchmarks at the earthquake timescale to demonstrate the effectiveness of our approach. We then discuss how these high-resolution models degrade if the time-step cannot capture the rupture process accurately and, from this, infer when it is important to consider coupling of the two timescales and the level of accuracy required. To build upon these benchmarks, we undertake a generic study of a thrust fault in the crust with a prescribed geometry. It is found that lower crustal rheology affects the periodic time of characteristic earthquake cycles and the inter-seismic, free-surface deformation rate. In particular, the relaxation of the surface of a cratonic region (with a relatively strong lower crust) has a characteristic double-peaked uplift profile that persists for thousands of years after a major slip event. This pattern might be diagnostic of active faults in cratonic regions.

Plain Language Summary The numerical modeling method for long-term tectonic deformations averages out the co-seismic fault displacement into thousands to tens of thousands of years, and neglects near-fault damages of earthquakes; therefore, it may not be able to decipher fault activities in detail. Software simulating earthquake rupture dynamics may not have a good estimation of background stress due to long-term tectonic deformations. In this study, we develop a numerical framework that embeds earthquake rupture dynamics into a long-term tectonic deformation model by adding inertial terms and using highly adaptive time-stepping that can capture deformation at plate-motion rates as well as individual earthquakes. The inertia term, which is neglected in long-term large-scale modeling methods, is considered to simulate the dynamic rupture processes. The rate-and-state frictional relationship for co-seismic fault slip is implemented in viscoelastic-plastic earth. Benchmarks of viscous flow, viscoelastic wave propagation and earthquake cycle simulations are tested. Based on these benchmarks, we undertake a generic study of a thrust fault in crust. We find that lower crustal rheology affects the periodic time of characteristic large earthquake cycles and the inter-seismic free surface movement. Cratons with a relatively strong lower crust due to lower temperature remain two peaks in surface uplift profiles around the fault zone for thousands of years after one characteristic earthquake, which help identify active faults in cratons.

1. Introduction

Numerical models assume different governing equations and constitutive relations depending on the dominant time- and length-scales for the problem. The timescales associated with changes in whole mantle flow are typically of the order of tens to hundreds of thousands of years and, as a result, it is usual to neglect the unimportant inertial terms and it is often unnecessary to consider the effects of elastic stresses. Such models are usually formulated on the assumption of creeping viscous flow following the Stokes equations (McKenzie, 1969). The dynamics of deformation within the lithosphere is dominated by localizing phenomena (shear banding and faulting) that are commonly modeled with visco-elastic-plastic rheology (Moresi et al., 2007). These models require significantly higher spatial and temporal resolution compared to whole-mantle flow models to capture the

10.1029/2023GC010872

Methodology: Haibin Yang, Louis Moresi, Julian Giordani
Project Administration: Louis Moresi
Resources: Louis Moresi
Software: Haibin Yang, Louis Moresi, Julian Giordani
Supervision: Louis Moresi, Huihui Weng, Julian Giordani
Validation: Haibin Yang
Visualization: Haibin Yang
Writing – original draft: Haibin Yang
Writing – review & editing: Haibin Yang, Louis Moresi, Huihui Weng

stress-redistribution that is associated with the creation, propagation of localized structures and the offsets that occur along their length. Plastic models of localization assume a static equilibrium with any time-dependence resulting from the evolution of damage variables or geometry (e.g., interfaces, surface topography). By contrast, at the shorter timescales associated with the individual ruptures of a fault, the largest terms in the equation of motion come from accelerations and the elastic response of the medium (Ben-Zion & Rice, 1993; Lapusta et al., 2000; Rice, 1993).

Fault zones are one of the structural units of the dynamic Earth that are challenging for simulations. Faults accumulate finite strain in deep ductile earth over years or longer and suddenly release stored elastic energy in shallow brittle earth through earthquake ruptures, which cause permanent displacements on the surface. The displacement of faults in long-term tectonic models are averaged over one time step of several millenniums, which approximates the cyclic accumulation of earthquake events. Faults designed in long-term tectonic models have a finite thickness and are free to deform in geometries, especially for modeling with the Particle-in-cell method (Harlow, 1964; Moresi et al., 2003; Yang, Moresi, & Mansour, 2021). The long-term tectonic models are driven by speculated external boundary conditions and internal body forces and can evolve in a self-consistent fashion. Conventional models using spectral boundary element method to simulate earthquake kinetics treat earthquake-holding faults as infinite thin interfaces that are confined to a specific geometry which may not evolve with time (Lapusta et al., 2000; Lapusta & Liu, 2009). The conventional short-term model focuses on one specific earthquake event rather than earthquake cycles. Recent developments with the finite difference, finite element, spectral element, and hybrid methods can flexibly incorporate complex fault geometries at greater computational costs than the boundary element methods, which often assume a damped inertia (i.e., "quasi-dynamic" earthquakes) (Jiang et al., 2022 and references therein). How one fault evolves in response to surface processes and mantle dynamics or interacts with each other in a system is rarely studied (Sobolev & Muldashev, 2017; K. Wang et al., 2012), especially in a full three-dimensional (3D) environment.

To cover the full spectrum of faulting behaviors, one should model both the short- and long-term dynamics. In the past decade, several experiments from the long-term tectonic modeling community have been conducted to develop feasible adaptive models for earthquake-cycle simulation with time steps ranging from sub-seconds to years with viscoelastic materials. Van Dinther, Gerya, Dalguer, Mai, et al. (2013) adopted the two-dimensional (2D) thermomechanical code I2ELVIS using an implicit, conservative finite difference scheme for incompressible medium (Gerya & Yuen, 2007). This 2D code was further developed for compressible medium by Herrendörfer et al. (2018). On the other hand, Sobolev and Muldashev (2017) develop a similar 2D seismo-thermo-mechanical approach based on SLIM3D (Popov & Sobolev, 2008), which is a thermomechanical finite element code for long-term tectonic modeling, but their experiments limit the minimum modeled time step to minutes such that the generation of seismic waves are not studied in their models. Different from previous applications of seismo-thermomechanical models, an elastoplastic code focusing on the shallow brittle part of earth crust was developed by Biemiller and Lavier (2017) to study earthquake cycles of normal faults. Unlike previous modeling of earthquake cycles (Lapusta et al., 2000; Rice, 1993), which assumes fault as an infinite thin interface, experiments developed by Biemiller and Lavier (2017) also allow fault to have a finite thickness as those long-term tectonic models, which have advantages in modeling internal structure evolution of a fault zone.

The frictional constitutive relation is a key factor controlling faulting features. A simplified friction relationship assuming linear decay of friction with steady state velocity was used by Van Dinther, Gerya, Dalguer, Mai, et al. (2013), following previous studies (Ampuero & Ben-Zion, 2008; Burridge & Knopoff, 1967; Cochard & Madariaga, 1994). Instead, Biemiller and Lavier (2017), Herrendörfer et al. (2018) and Sobolev and Muldashev (2017) use the classical rate-and-state friction (Dieterich, 1978, 1979; Ruina, 1983), which assumes a logarithmic dependence of friction with slip rate. Note that the rate-and-state dependent friction relationship does not include the fracturing mechanism for fault evolution; Tong and Lavier (2018) develop a new frictional relationship which depends on the historical damage in the fault zone to model quasi-dynamic rupture processes.

In this paper, we discuss our approach to include inertial terms into the open-source Underworld geodynamics modeling framework (Mansour et al., 2020; Moresi et al., 2007). This code was originally designed to address coupled problems in mantle-lithosphere dynamics using a history-dependent, viscoelastic-plastic formulation of the Stokes equations with a particle-in-cell approach to track elastic stresses during fluid deformation (Farrington et al., 2014; Moresi et al., 2002). Fluid acceleration can also be tracked using the Lagrangian particle swarm, which we demonstrate through a series of standard benchmarks of the Navier-Stokes problem.

A second benchmark is to compare the speed of a shear-wave through a viscoelastic medium for which analytic solutions are available. In addition, we compare this code with the community code verification exercise for 3D dynamic modeling of sequences of earthquakes and aseismic slip (Jiang et al., 2022). We finally apply our new 3D code for generic models of inter-seismic deformation of thrust faults and discuss how we can use surface geodetic observations to infer the strength of the lower crust and activity of faults in stable cratons.

2. Methods

2.1. Governing Equations

We start with the equations for the conservation of momentum (Equation 1a) and mass (incompressible material, Equation 1b),

$$\frac{\partial \tau_{ij}}{\partial x_j} - \frac{\partial p}{\partial x_i} = -\rho g_i + \rho \frac{D v_i}{D t} \tag{1a}$$

$$\frac{\partial v_i}{\partial x_i} = 0 \tag{1b}$$

where τ_{ij} is deviatoric stress, p is pressure, g_i is gravitational acceleration, ρ is density, v_i is velocity, i and j are coordinate indices and x_i and x_j denote spatial coordinates. $\rho \frac{Dv_i}{Dt}$ is the inertia term, which is negligible in long-term tectonic modeling but needs to be considered in this study. The material derivative $\frac{Dv_i}{Dt}$ is local time rate of change in the reference frame that moves with the fluid.

2.2. Constitutive Relationship and Numerical Approximations

Underworld is implemented as a suite of different modules (Moresi et al., 2007), which can be flexibly modified to solve elliptic momentum equations. In this section, we show how we use the finite difference approximation for the history dependent term to make it conform with classic Underworld implementation. Other details of the basic computational approaches used in Underworld are listed in previous studies by Moresi et al. (2002, 2003, 2007).

2.2.1. Inertia Term

In the particle-in-cell method with Lagrangian particles moving between cells (Moresi et al., 2003), the material derivative of velocity is equal to the time derivative recorded on the material points, and can be approximated by a finite difference expression such as

$$\frac{D v_i}{D t} = \frac{v_i - v_i^{t-\Delta t}}{\Delta t}, \tag{2}$$

where Δt is the time interval between the present time, t, and the previous time, $t - \Delta t$; $v_i^{t-\Delta t}$ is the particle velocity from the previous time-step recorded at the location of the particle at $t - \Delta t$ (Gerya, 2019). The mesh-based velocity field is used to update the positions of particles after a timestep and interpolated to determine the velocity history-variables.

For a viscous material, the constitutive relationship gives

$$\tau_{ij} = 2\eta \dot{\varepsilon}_{ij} = \eta \left(\frac{\partial v_i}{\partial x_j} + \frac{\partial v_j}{\partial x_i} \right), \tag{3}$$

where η is the viscosity and $\dot{\varepsilon}_{ij}$ is the strain rate. Substituting Equations 2 and 3 into Equation 1a, we obtain

$$\frac{\partial}{\partial x_j} \left[\eta \left(\frac{\partial v_i}{\partial x_j} + \frac{\partial v_j}{\partial x_i} \right) \right] - \frac{\rho v_i}{\Delta t} - \frac{\partial p}{\partial x_i} = -\rho g_i + \rho \frac{-v_i^{t-\Delta t}}{\Delta t}. \tag{4}$$

The unknowns v_i and p can be solved with the combination with Equation 1b (Moresi et al., 2003).

2.2.2. Maxwell Viscoelastic Constitutive Equations

The Maxwell material assumes that the strain rate tensor, $\dot{\varepsilon}_{ij}$, is a sum of an elastic strain rate tensor, $\dot{\varepsilon}_{ij}^{e}$, and a viscous strain rate tensor, $\dot{\varepsilon}_{ij}^{v}$:

$$\dot{\varepsilon}_{ij} = \dot{\varepsilon}_{ij}^{e} + \dot{\varepsilon}_{ij}^{v} = \frac{\dot{\tau}_{ij}}{2G} + \frac{\tau_{ij}}{2\eta}, \tag{5}$$

where G is shear modulus. Writing the material derivative of stress $\dot{\tau}_{ij}$, which is a local time rate of change of stress, in form of an approximate difference:

$$\dot{\tau}_{ij} \approx \frac{\tau_{ij} - \tau_{ij}^{t-\Delta t}}{\Delta t} \tag{6}$$

gives

$$\tau_{ij} = 2\frac{\eta G \Delta t}{\eta + G\Delta t}\left[\dot{\varepsilon}_{ij} + \frac{\tau_{ij}^{t-\Delta t}}{2G\Delta t}\right], \tag{7}$$

where τ is the stress at current time, t, and the stress $\tau^{t-\Delta t}$ at earlier time, $t - \Delta t$. Equation 7 can be written in the form of Equation 3

$$\tau_{ij} = 2\eta^{\mathrm{ve}}\dot{\varepsilon}_{ij}^{\mathrm{ve}}, \tag{8}$$

where

$$\eta^{\mathrm{ve}} = \frac{\eta G\Delta t}{\eta + G\Delta t}, \tag{9}$$

$$\dot{\varepsilon}_{ij}^{\mathrm{ve}} = \dot{\varepsilon}_{ij} + \frac{\tau_{ij}^{t-\Delta t}}{2G\Delta t}. \tag{10}$$

Substituting Equation 8 into Equation 1a leads to

$$\frac{\partial}{\partial x_j}\left[\eta^{\mathrm{ve}}\left(\frac{\partial v_i}{\partial x_j} + \frac{\partial v_j}{\partial x_i}\right)\right] - \frac{\partial p}{\partial x_i} = -\rho g_i + \rho\frac{Dv_i}{Dt} - \frac{\eta^{\mathrm{ve}}}{G\Delta t}\frac{\partial}{\partial x_j}\tau_{ij}^{t-\Delta t}, \tag{11}$$

The $\frac{Dv_i}{Dt}$ can be substituted with Equation 2.

2.2.3. Second-Order Approximation of Time Derivative

The first-order finite difference approximation of time derivative is used for the velocity acceleration (Equation 2) and stress rate (Equation 6). To increase the numerical accuracy, a second-order method is also investigated in this study.

The second-order finite difference approximation for the velocity acceleration is written as

$$\frac{Dv_i}{Dt} \approx \varphi\frac{v_i^{t+\Delta t} - v_i}{\Delta t} + (1-\varphi)\frac{v_i - v_i^{t-\Delta t}}{\Delta t}, \tag{12}$$

where $v_i^{t+\Delta t}$ is the particle velocity from the further time step $t + \Delta t$; φ and $1 - \varphi$ is the weight for the estimated velocity acceleration in the forward and backward time step, respectively. Accordingly, Equation 4 has an updated expression:

$$\frac{\partial}{\partial x_j}\left[\eta\left(\frac{\partial v_i}{\partial x_j} + \frac{\partial v_j}{\partial x_i}\right)\right] - \frac{\rho(1-2\varphi)v_i}{\Delta t} - \frac{\partial p}{\partial x_i} = -\rho\left[g_i - \left(\varphi\frac{v_i^{t+\Delta t}}{\Delta t} - (1-\varphi)\frac{v_i^{t-\Delta t}}{\Delta t}\right)\right]. \tag{13}$$

Similarly, Equation 6 has the following higher order form:

$$\dot{\tau}_{ij} \approx \varphi\frac{\tau_{ij}^{t+\Delta t} - \tau_{ij}}{\Delta t} + (1-\varphi)\frac{\tau_{ij} - \tau_{ij}^{t-\Delta t}}{\Delta t} \tag{14}$$

where $\tau_{ij}^{t+\Delta t}$ is the deviatoric stress tensor from the further time step. With Equation 14, the viscoelastic viscosity and strain rate in Equations 9 and 10 is modified as

$$\eta^{\mathrm{ve}} = \frac{\eta G \Delta t}{(1-2\varphi)\eta + G\Delta t}, \tag{15}$$

$$\dot{\varepsilon}_{ij}^{\mathrm{ve}} = \dot{\varepsilon}_{ij} + \frac{(1-\varphi)\tau_{ij}^{t-\Delta t} - \varphi\tau_{ij}^{t+\Delta t}}{2G\Delta t}. \tag{16}$$

We have the similar final form

$$\begin{aligned} &\frac{\partial}{\partial x_j}\left[\eta^{\mathrm{ve}}\left(\frac{\partial v_i}{\partial x_j} + \frac{\partial v_j}{\partial x_i}\right)\right] - \frac{\rho(1-2\varphi)v_i}{\Delta t} - \\ &\frac{\partial p}{\partial x_i} = -\rho\left[g_i - \left[\varphi\frac{v_i^{t+\Delta t}}{\Delta t} - (1-\varphi)\frac{v_i^{t-\Delta t}}{\Delta t}\right]\right] \\ &-\frac{\eta^{\mathrm{ve}}}{G\Delta t}\frac{\partial}{\partial x_j}\left[(1-\varphi)\tau_{ij}^{t-\Delta t} - \varphi\tau_{ij}^{t+\Delta t}\right] \end{aligned} \tag{17}$$

We note that if $\varphi = 0$, Equation 12 is the same as Equation 2, Equation 14 is equal to Equation 6 and the viscoelastic viscosity and strain rate in Equations 15 and 16 equals Equations 9 and 10. For the second order approximation, the stress and velocity from the further time step is required as a priori to calculate solutions at current time step. We must predict one value for the further time step and then use this prediction to solve the problem at current time step, the solution of which is used to evaluate the further time step as well. The prediction and correction are conducted iteratively until the solution converges. As the prediction of the forward time step is in lower accuracy than the backward one, the weight φ for the forward calculation should be less than the weight $(1-\varphi)$ for the backward calculation, thus leading to $\varphi < 0.5$. We can estimate the further time step by solving the Navier-Stokes equation with a first-order approximation and then correct it with the current time step solution, which is obtained by the second order method. Alternatively, regarding the prediction of further time step, we may use polynomial functions to fit historical values at $t-\Delta t, t-2\Delta t, t-3\Delta t \ldots, t-n\Delta t$, where n is an integer number, and extrapolate the value at $t+\Delta t$. This can be implemented following the Adams-Bashforth method (Durran, 1991). The complexity of this polynomial function depends on how many historical values are used. The first one is taken in this study. $\varphi = 0$ (first order approximation of time derivative) is used in most cases of this study, and a nonzero value of φ is discussed in Section 3.2.

2.2.4. Yield Strength for Long-Term Deformation

The Drucker-Prager yield model is used to simulate long-term fault behavior:

$$\tau_{\mathrm{II}} < \tau_{\mathrm{yield}} = \mu_{\mathrm{st}}^{*} p + C, \tag{18}$$

where τ_{II} is the second invariant of the stress tensor τ_{ij} and its upper limit is τ_{yield}, C is rock cohesion and μ_{st}^{*} is static friction coefficient commonly used in long-term deformation. With the plastic deformation, the plastic strain rate tensor $\dot{\varepsilon}_{ij}^{p}$ needs to be added to Equation 5:

$$\dot{\varepsilon}_{ij} = \dot{\varepsilon}_{ij}^{e} + \dot{\varepsilon}_{ij}^{v} + \dot{\varepsilon}_{ij}^{p}. \tag{19}$$

The composite visco-elastic-plastic flow material is modeled with an effective viscosity:

$$\eta_{\mathrm{vep}} = \min\left(\eta^{\mathrm{ve}}, \frac{\tau_{\mathrm{yield}}}{2\dot{\varepsilon}_{II}^{\mathrm{ve}}}\right), \tag{20}$$

where the $\dot{\varepsilon}_{\mathrm{II}}^{\mathrm{ve}}$ is the second invariant of the effective strain rate in Equation 10.

2.2.5. Rate-And-State Frictional Relationship

For the short-term deformation, for example, the earthquake rupture time scale (seconds to minutes), the rate-and-state frictional (RSF) relationship is commonly used in earthquake rupture simulations (Dieterich, 1978, 1979; Ruina, 1983). The dynamic friction coefficient

$$\mu^{*} = \mu_{\mathrm{st}}^{*} + a\ln\left(\frac{V}{V_0}\right) + b\ln\left(\frac{\theta V_0}{D_{\mathrm{RS}}}\right), \tag{21}$$

where a and b are nondimensional parameters, V is the slip rate on the fault, D_{RS} is the characteristic slip distance, θ is the state variable, μ_{st}^{*} and V_0 are the reference static friction coefficient and the magnitude of the reference fault slip rate, respectively. $a - b < 0$ represents velocity-weakening (VW) material, in which earthquake nucleation is favored; $a - b > 0$ represents a velocity-strengthening (VS) material which tends to discourage slip instability. The evolution of state θ is a function of slip rate V and critical slip distance D_{RS}:

$$\frac{d\theta}{dt} = 1 - \frac{\theta V}{D_{\mathrm{RS}}}. \tag{22}$$

If the slip rate V is constant over a time step, Equation 22 can be integrated to obtain the analytical solution and define θ^t as the value of the state variable at the current time, with the state variable $\theta^{t-\Delta t}$ at the previous time step:

$$\theta^t = \frac{D_{\mathrm{RS}}}{V} + \left(\theta^{t-\Delta t} - \frac{D_{\mathrm{RS}}}{V}\right)e^{-\frac{\Delta t V}{D_{\mathrm{RS}}}}. \tag{23}$$

θ is updated after each time step with updated fault slip rate.

We note that faulting problems in seismic simulation and long-term tectonic modeling have different representation of fault planes. V in the RSF relationship in Equation 21 is taken as the fault slip rate on a predefined fault plane, which is assumed to be an infinitely thin interface. Instead, a fault represented in continuum mechanics (e.g., viscous mantle flow) has finite thickness and experiences volumetric deformation following the plastic rheology. Many previous studies have tried to link the RSF relationship to flow law in continuum mechanics (Noda & Shimamoto, 2010; Sleep, 1997), and the fault slip rate is approximated by $2\dot{\varepsilon}_{\mathrm{II}} w_f$, where $\dot{\varepsilon}_{\mathrm{II}}$ is the second invariant of the strain rate of the fault zone and the w_f is the fault zone width (Van Dinther, Gerya, Dalguer, Corbi, et al., 2013).

The fault shear strength in seismic simulation is evaluated by normal stress σ_n with respect to a predefined fault plane, whereas in the continuum approach, the invariant of the coordination system is commonly used to adapt to emergent fault evolution, where the normal stress is replaced by pressure (p) and the shear stress is replaced by second stress invariant (τ_{II}).

With the dynamic friction coefficient described in Equation 21, the yielding stress in Equation 18 can be written as

$$\tau_{\mathrm{II}} < \tau_{\mathrm{yield}} = \mu^* p + C. \tag{24}$$

Note that co-seismic slip rate is several orders of magnitude higher than the inter-seismic fault creep rate. The RSF relationship is conventionally used for co-seismic fault movement. In our numerical modeling, both the co-seismic and inter-seismic friction coefficient are modeled with the RSF relationship (Equation 21). That means, for the inter-seismic stage, the fault movement is in a quasi-equilibrium state with $\frac{dV}{dt} \approx 0$ and $\frac{d\theta}{dt} \approx 0$. If the slip rate $V \approx V_0$ and $V_0 = \frac{D_{\mathrm{RS}}}{\theta}$, $\mu^* = \mu^*_{\mathrm{st}}$ and the yielding stress in Equation 24 converges to Equation 18.

2.3. Adaptive Time Step

For long-term and short-term deformations, we calculate various time step limits and choose the minimum at each iteration. First, the time step should be smaller than the characteristic Maxwell relaxation time:

$$\Delta t_{\mathrm{ve}} = \frac{\eta}{G}. \tag{25}$$

Assuming $G = 3 \times 10^{10}$ Pa and ductile viscosity $\eta = 10^{20}$ Pas gives a relaxation time of ~100 years. For the viscoelastic-plastic deformation, the viscoplastic viscosity defined as (Herrendörfer et al., 2018)

$$\eta_{vp} = \eta \frac{\tau_{\mathrm{II}}}{2\eta\dot{\varepsilon}^p_{\mathrm{II}} + \tau_{\mathrm{II}}}, \tag{26}$$

where τ_{II} and $\dot{\varepsilon}^p_{\mathrm{II}}$ are the second invariant of the deviatoric stress and plastic strain rate, respectively. Note that if $\dot{\varepsilon}^p_{\mathrm{II}} = 0$, $\eta_{vp} = \eta$. Replacing η in Equation 25 with η_{vp} in Equation 26, we have

$$\Delta t_{\mathrm{vep}} = \frac{\eta_{vp}}{G}. \tag{27}$$

In addition, the selected time step is used for particle advection following the Courant-Friedrichs-Lewy (CFL) condition and the slip per time step is not allowed to be larger than the grid size Δx or Δy (Moresi et al., 2003):

$$\Delta t_{\mathrm{CFL}} = \min\left(\left|\frac{\Delta x}{v_x}\right|, \left|\frac{\Delta y}{v_y}\right|\right). \tag{28}$$

Then, we set a maximum time step allowed in one time step, Δt_{max}, which depends on the Maxwell relaxation time Δt_{ve} and is ca. 10–100s years used in this study.

Therefore, the minimum time step for the model is

$$\Delta t_0 = \min\left[\pounds\Delta t_{\text{vep}}, \Delta t_{\text{CFL}}, \Delta t_{\text{max}}\right], \tag{29}$$

where the pre-factor £ is a constant value and is set to be 0.2 in most cases in this study. As Δt appears as denominator in Equations 4, 11, and 17, too small Δt would make our solver unstable during nonlinear iteration; thus, we truncate the minimum time step by

$$\Delta t = \max[\Delta t_0, \Delta t_{\text{min}}], \tag{30}$$

and $\Delta t_{\text{min}} = 0.01$ s in most cases of this study, which is set to ensure $\Delta t \le \frac{D_{\text{RS}}}{V}$ during the initiation of the earthquake and to capture the weakening of the material (Rice, 1993), where the commonly used value for $D_{\text{RS}} > 0.01$ m to increase nucleation and cohesive zone size and reduce computational cost (while the laboratory measurements are smaller than 0.01 m) and the fault slip rate $V < \sim 1$ m/s. This is close to the implementation by Herrendörfer et al. (2018) and Lapusta et al. (2000) who limit the time step by $\Delta t_w = \beta \frac{D_{\text{RS}}}{V}$, where the pre-factor β ($\beta < 1$) is a constant. Herrendörfer et al. (2018) find Δt_w is very close to Δt_{vep} during co-seismic stages. We thus only consider Δt_{vep} in our study and use the pre-factor £ to tune the value of the viscoelastic-plastic relaxation time.

In some cases, we find too high ratio of time increasement between two sequential time steps, $\Delta t^k/\Delta t^{k-1}$, where k is the step number, would make the nonlinear iteration hard to converge. We tend to limit $0.25 < \Delta t^k/\Delta t^{k-1} < 4$. Similar approach is also applied in the study of Rice (1993). Time stepping procedures are critical to seismic cycle simulations, and more discussion on the strategy is introduced in Section 3.3.

2.4. Particle Advection

With the particle-in-cell method, Lagrangian particles carrying various properties, for example, the stress at previous time step, to move in Eulerian meshes. The Lagrangian reference frame equates the material derivative with the time derivative. All rates change with time are evaluated particle by particle and updated during the advection phase. The particle position can be updated with velocity interpolated from mesh nodes. A higher order advection scheme like the fourth order Runge-Kutta method provides more accurate results. It can be done in a predictor-corrector way, that is, first updating particle positions to obtain velocity solutions and then iteratively modifying final positions to have a converged velocity. The improvements in accuracy from repeatedly updating of the particle location are found to be too small to justify the increase in complexity, but cost in computation. In practice, the second order Runge-Kutta scheme, that is, the mid-point method is preferred and appropriately reducing time step size is an alternative way to promote a higher accuracy (see examples in Section 3.2).

3. Benchmarks

In this section, several benchmarks are investigated to demonstrate the effectiveness of our code in modeling coupled simulations: (a) time-dependent viscous flow compared with published numerical solutions, (b) analytical solutions for viscoelastic wave propagation and (c) community model of earthquake cycle simulations.

3.1. Time-Dependent Viscous Flow

The inertia term is important in earthquake dynamic rupture processes, which can reach the same order of magnitude as gravity acceleration but is neglected in long-term tectonic modeling. We first test the implemented inertia term (Equation 1) with published numerical results from Kolomenskiy and Schneider (2009), which is a fluid-solid interaction model where an infinite-long solid cylinder body falls perpendicularly to its longitudinal axis. The modeled fluid has dimensionless viscosity $\eta = 0.03926$, density $\rho = 1$, solid cylinder density $\rho_s = 2$, gravity acceleration $g = 9.81$ and the diameter of the cylinder $D = 1$. The model size is $Lx \times Ly = 10 \times 40$, and different model resolutions of 512×2058, 256×1024, 128×252 and 64×256 quadrilateral bilinear elements are tested for comparison. The cylinder starts from rest and then speeds up its falling speed due to gravity before reaching a steady state (Figure 1).

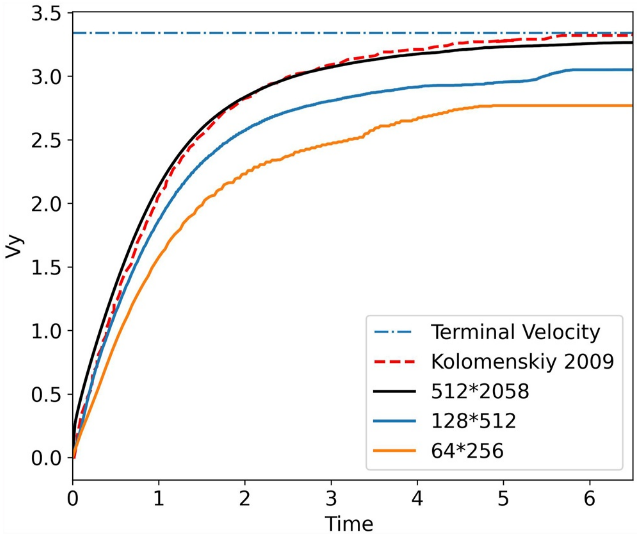

Figure 1. Velocity of a falling cylinder starting from rest to steady state. The horizontal line at $Vy = 3.34$ marks the terminal velocity. The red dashed line is the result from Kolomenskiy and Schneider (2009). Solid lines with different mesh resolutions are from Underworld.

Considering the balance between drag and buoyance-corrected weight, the terminal steady state velocity u_t can be estimated by

$$C_d \frac{\rho u_t^2}{2} D + (\rho - \rho_s) g \frac{\pi D^2}{4} = 0, \tag{31}$$

where C_d is the drag coefficient, which is a function of Reynolds number, $\mathrm{Re}\left(= \frac{\rho u_t D}{\eta}\right)$, for a cylinder falling in a steady inflow.

The choice of parameters gives a terminal velocity $u_t = 3.34$ with the corresponding Re = 85. Our numerical models with high mesh resolution also agree with this estimated terminal velocity (Figure 1) to within 5% for the same mesh resolution (512 × 2058). The high-resolution models are also comparable to results from Kolomenskiy and Schneider (2009). Reducing mesh resolution also reduces the modeled falling velocity. The terminal velocity is dropped by ∼20% when the mesh resolution is reduced by a factor of 8.

For the viscous inertia flow that can generate eddies, the Re is estimated to be >∼10. We test a group of benchmarks with Re = 40–2000 to see how well our numerical results are matched by published solutions in a quantitative fashion. Here we introduce another dimensionless parameter Strouhal number, $\mathrm{St} = fD/U$, where f is the frequency of vortex shedding, D is the characteristic length (e.g., the diameter of the falling cylinder in above mentioned experiment), and U the fluid velocity. No analytical solutions are available for the comparison, but many studies have provided different approximations of St for Re of different ranges (Fey et al., 1998; Williamson & Brown, 1998). Our numerical results are visually comparable with previous studies (Figure 2). We note that the precision of modeling results depends on the mesh resolution as shown in Figure 1. That is because high Re produces very small-scale eddies to dissipate the energy, thus requiring higher mesh resolution to capture more detailed structures. Examples of two cases with Re = 40 and 400 are shown in Supporting Information S1 as videos. As flow passes a fixed cylinder, the vortical wake develops for high Re values, and it is unstable and forms the von Karman vortex street due to oscillating forces (see Movie S1 and Movie S2).

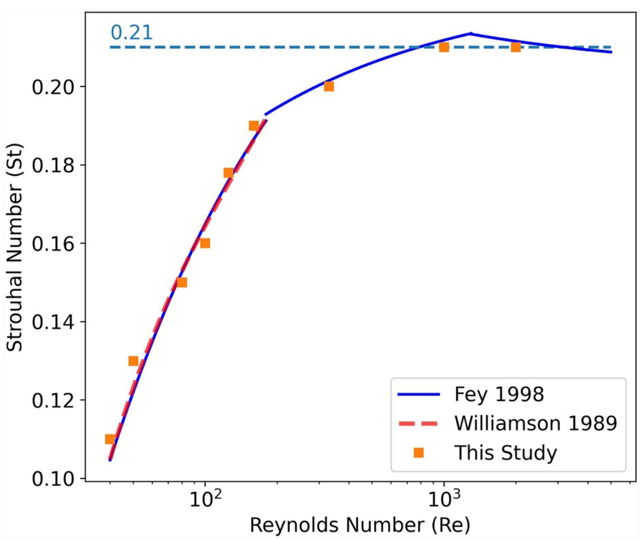

Figure 2. The Strouhal number versus Reynolds number. Note that the estimation from Williamson and Brown (1998) almost overlaps with Fey et al. (1998) in the range of 40–150. For 10,000 > Re > 200, the Strouhal number is estimated to be around 0.21.

3.2. Viscoelastic Wave Radiation

During the dynamic earthquake rupture propagation, the stored elastic energy is partly released by elastic wave propagation. The radiated seismic waves have also been demonstrated to trigger earthquake events on distant faults when the triggering stress is higher than the required fault failure stress (Brodsky and van der Elst, 2014). We evaluate how well the dynamic stress changes, after a wave passes through, can be described by our numerical model.

Here we consider a simple case, an infinite long rod made up of a linear Maxwell material and the x coordinate is measured along the rod length. A 2D numerical model with high aspect ratio is used to simulate the infinite long rod. The model size $Lx \times Ly$ = 1100 m × 4.68 m is simulated with 800 × 3 quadrilateral quadratic elements. The periodic boundary condition is applied in y direction. Initially, the rod is unstrained and at rest, and then it is subjected to a constant shear velocity V at one end $x = 0$. The analytical solution for stress $\sigma(x, t)$ is provided by Lee and Kanter (1953),

$$\sigma = -\rho c V e^{-\left(\frac{\gamma G}{2}\right)t} I_o\left[\frac{\gamma G}{2}\left(t^2 - \frac{x^2}{c^2}\right)^{\frac{1}{2}}\right] H\left(t - \frac{x}{c}\right), \tag{32}$$

where I_o is the Bessel function of imaginary argument and H is the Heaviside step function, γ is the reciprocal of the viscosity, G is the shear modulus, and $c^2 = G/\rho$. We scale the time by characteristic relaxation time, $\tau = t/\tau_0 = t\gamma G$, and the distance by $\xi = \gamma G x/c = x/c\tau_0$, and Equation 32 becomes

10.1029/2023GC010872

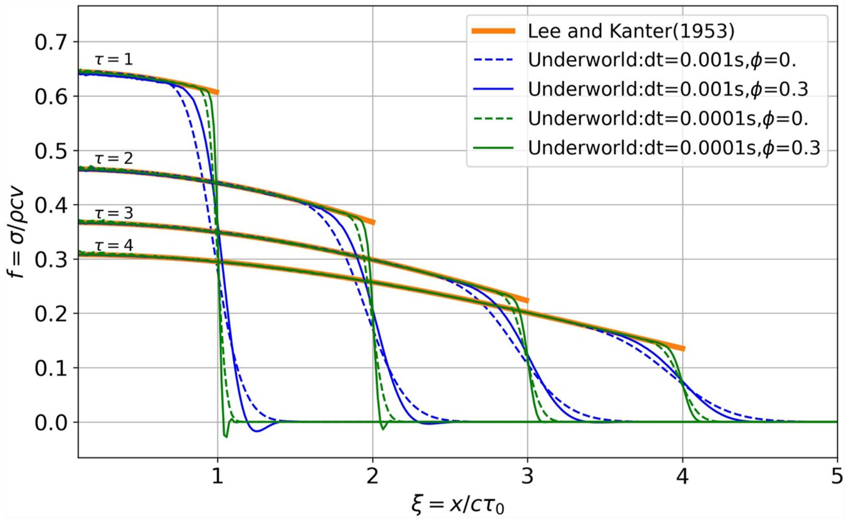

Figure 3. Wave propagation along a Maxwell rod. The dimensionless stress f is plotted against dimensionless distance ξ for the dimensionless time τ between 0 and 8. The solid orange thick orange line is an analytical solution from Lee and Kanter (1953) while other blue and green lines are produced by Underworld for different temporal resolutions (dt) and truncation precisions (φ). The dimensionless stress is described by the Heaviside step function. And when the wave front reaches $\xi = 1$ at $\tau = 1$, and the stress is zero ahead of this front ($\xi > 1$).

$$-\frac{\sigma}{\rho c V} = f = e^{-\frac{\tau}{2}} I_0\left[\frac{1}{2}\left(\tau^2 - \xi^2\right) H(\tau - \xi)\right]. \tag{33}$$

In Figure 3, the dimensionless stress f is plotted against dimensionless distance ξ for the dimensionless time τ between 0 and 8 and it illustrates the propagation and decay of the stress wave from the shear end of the rod in the case of a Maxwell material in dimensionless units. The Heaviside step function H shows the wave front is at $\tau = \xi$, and the stress is zero ahead of this front. If the unit velocity of the wave front in the (ξ, τ) system is transformed back into the physical (x, t) system, the front of the disturbance moves with the elastic wave velocity c. Note that a wave of stress discontinuity of amplitude $-\rho c V$ sets out from shear boundary $x = 0$, and the stress discontinuity is of magnitude $-\rho c V e^{-\xi/2}$ when it reaches ξ. That is, the stress magnitude dies out exponentially as wave progresses and the stress at the shear boundary $x = 0$ also falls off as the duration of shearing increases.

Comparing our results with the analytical solution, we find our numerical solution well describes the stress field behind the wave front and disperses at the stress discontinuity (Figure 3), especially for the first order approximations ($\varphi = 0$). The dispersion effect of the wave front makes it difficult to pick the arrival time of seismic waves, thus making it hard to determine the seismic wave velocity. To roughly estimate the seismic wave velocity, the wave front is better represented by the time that corresponds the maximum of the stress derivative with time ($\xi = 1, 2, 3 \ldots n$, and n is an integer number; Figure 3).

This dispersion effect can be damped by using higher-order time derivative approximations with iterative prediction and corrections or reducing the time step at the cost of computational time to produce steeper stress profile at wave front (Figure 3). For the second order method, the stress overshoot appears at the wave front when $\tau = 1$ and 2. We therefore tend to use the first order approximations in following studies as it is more stable than the second order method.

3.3. 3D Model Simulation of Earthquake Cycles With the RSF

To further benchmark this code, we compare it with the community benchmark model BP5 (Jiang et al., 2022) for three-dimensional dynamic modeling of sequences of earthquakes and aseismic slip (3D SEAS) simulations. Adding the inertia term in the momentum balance equation (Equation 1a) and using the Maxwell material (Equation 5), our code can simulate earthquake cycles for brittle materials by implementing artificially high viscosity ($>10^{25}$ Pas) of long relaxation time (>1 million years). Full descriptions of this benchmark are available online

10.1029/2023GC010872

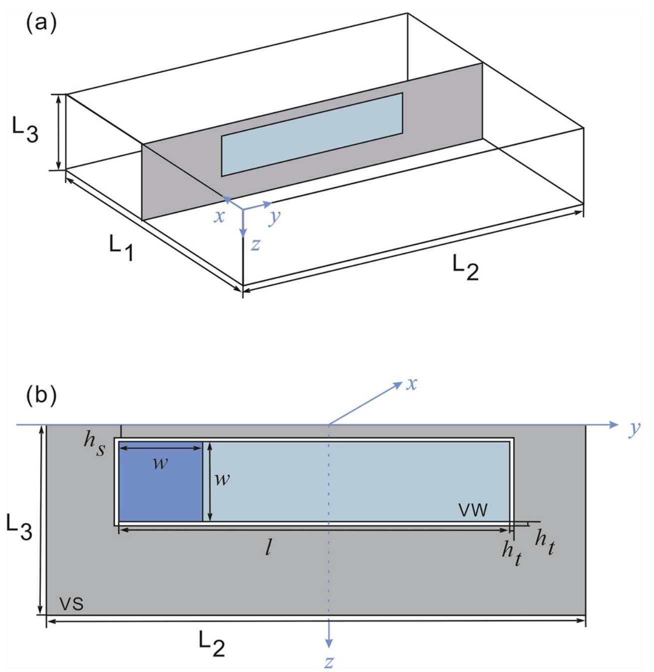

Figure 4. The benchmark model BP5 for 3D sequence of earthquakes and aseismic slip modeling. (a) A vertical planar fault is embedded in the middle of a homogenous, isotropic half-space with a free surface at $z = 0$. Fault behavior is controlled by the rate-and-state friction law. A periodic boundary condition is applied in y direction. (b) The velocity-weakening (VW) region (dark and light blue) is located within a transition zone (white), outside of which is the velocity-strengthening (VS) region (gray). In y and z directions, the frictional domain and VW region are ($L2$, $L3$) and (l, w), respectively. An initial nucleation zone (dark blue square with a width of w) is designed at the left end of the VW region.

on the SEAS code comparison platform (https://strike.scec.org/cvws/seas/), and here we give a brief introduction.

A vertical, strike-slip fault is embedded in the central part of a homogeneous and isotropic half-space, with a free surface $z = 0$ (Figure 4). The finite width of the fault (w_f) is of one element size in x direction, starting from $x = 0$ and ending in $x = \Delta x$, where Δx is the one mesh size in x direction. This setup makes the fault conform to the mesh, and no mixed material in one element affects the stress estimation (Yang, Moresi, & Mansour, 2021). The fault-normal, along-strike and along-dip dimensions of the computational model are marked as $L1$, $L2$, and $L3$, respectively. A constant rate V_L is applied at the bottom of the model across the finite fault zone and a constant fault-parallel velocity ($\pm½\ V_L$) is also applied at the far field of the fault at $x = \pm½\ L1$. To achieve a spatially uniform distribution of fault slip rates, the initial state over the entire fault zone is prescribed with the steady-state value at the initiate slip rate V_{init}, that is $\theta_0 = \frac{D_{\text{RS}}}{V_{\text{init}}}$. The corresponding steady-state pre-stress τ^0 is

$$\tau^0 = a\sigma_n \text{arcsinh}\left[\frac{V_{\text{init}}}{2V_0}\exp\left(\frac{\mu_0 + b\ln\left(\frac{V_0}{V_{\text{init}}}\right)}{a}\right)\right]. \tag{34}$$

A nucleation location for the first event is designed to break the lateral symmetry of the fault and facilitate code comparisons. The nucleation zone is located within the VW region with a width of $w = 12$ km and a center at (-24, -10 km). In this nucleation zone, a higher initial slip rate V_i is applied in y direction at $t = 0$, and the initial state variable θ_0 is kept unchanged, thus producing a higher pre-stress by replacing V_{init} with V_i in Equation 34.

There are two critical length scales in earthquake dynamics: the cohesive zone and the nucleation zone. The former describes the spatial region near the rupture front where the breakdown of fault resistance occurs and shrinks as rupture propagates (Palmer & Rice, 1973) and the latter describes the minimum region for spontaneous nucleation on a fault controlled by VW friction (Rice & Ruina, 1983; Rubin & Ampuero, 2005). For rate-and-state friction law, the static cohesive zone Λ_0 is estimated as follows (Day et al., 2005; Lapusta & Liu, 2009):

$$\Lambda_0 = C\frac{GD_{\text{RS}}}{b\sigma_n}, \tag{35}$$

where C is a pre-factor of order 1. And the size of the nucleation zone is estimated for the aging law for $0.5 < a/b < 1$ as follows (Chen & Lapusta, 2009):

$$h = \frac{\pi}{2}\frac{GbD_{\text{RS}}}{(b-a)^2\sigma_n}. \tag{36}$$

The calculated cohesive zone and nucleation zone for the BP5 benchmark model are 5.6 and 12.5 km, respectively. To have sufficient resolution, we use ~1000 m as the grid size in low-order accuracy for BP5, which resolves the cohesive zone with no less than four cells, as suggested by Day et al. (2005).

The BP5 benchmark (Table 1) is first simulated with a reference model size of 96 km ($L1$) × 100 km ($L2$) × 30 km ($L3$) by 128 × 64 × 64 quadrilateral bilinear elements. Results from the SEAS code comparison platform (https://strike.scec.org/cvws/seas/) with the mesh resolution of 1000 m are selected for comparison in this study (Table 2). The stress at a depth of 10 km in the middle point along the fault strike ($y = 0$) and the maximum slip rate along the entire fault are tracked for comparison (Figure 5). 0.1 m/s is taken as a threshold of fault slip rate to mark the earthquake initiation. In case of long-term fault behavior, the period of earthquake cycles in Underworld is ~260 years, which is longer than other published results of ~230 years but is very close to the estimation from EQsimu. Both Underworld and EQsimu use the finite element method while other codes are based either on the

Table 1
Parameters in Benchmark Model BP5

Parameter	Symbol	Value in BP5
Density	ρ	2670 kg/m^3
Shear wave speed	Cs	3.464 km/s
Effective normal stress	σ_n	25 MPa
Characteristic state evolution distance	D_{RS}	0.14 m/0.13 m (nucleation zone)
Rate-and-state parameter, VW	a	0.004
Rate-and-state parameter, VS	a	0.04
Rate-and-state parameter, VW & VS	b	0.03
Reference slip rate	V_0	10^{-6} m/s
Reference coefficient of friction	μ^*_{st}	0.6
Plate loading rate	V_L	10^{-9} m/s
Initial slip rate	V_{init}	10^{-9} m/s
Initial slip rate in nucleation zone	V_i	0.03 m/s
VW-VS transition zone width	h_t	2 km
VW zone width	w	12 km
VW zone length	l	60 km
Shallow VS region width	h_s	2 km
Nucleation zone width	w	12 km

(spectral) boundary element method or the finite-difference method (i.e., GARNET). The stress drop after each event is ~10 MPa and is consistent with all other results.

Regarding the short-term behavior, the stress and slip rate at the reference point (0, 0, −10 km) are investigated (Figure 6). The rupture propagation speed in Underworld is much faster than other results. The estimated time of earthquake rupture propagation from the nucleation zone to the reference point is ~5 s in the Underworld models, and ~20 s in the other quasi-static models. The fast rupture propagation in Underworld may be attributed to two reasons. First, other models consider quasi-static situations while Underworld is fully dynamic modeling. The fully dynamic modeling can produce faster rupture propagations than quasi-static models (Jiang et al., 2022; Thomas et al., 2014), as is also evidenced by the fully dynamic results with BICyclE (dashed lines in Figure 6) which is about 10 s faster than the quasi-static models. The other major difference is that Underworld assumes an incompressible medium while all other codes assume a compressible medium. An incompressible medium is also found to produce faster rupture propagation rate than a compressible medium for fully dynamic modeling (see Figure 17d in Herrendörfer et al. (2018)) as the rigidity of an incompressible medium cannot distribute stress by volumetric deformation, thus increasing stress at the rupture front and the rupture propagation rate.

Both the long-term and short-term fault slip evolution is recorded by vertical (Figure 7) and horizontal (Figure 8) profiles. The maximum co-seismic slip for each event is ~7 m and consistent with published results (Jiang et al., 2022). The designed weak zone at $y = -30$ to 18 km can nuclearize the initial earthquake rupture (Figure 8) for the first event but fails in the sequential events. Comparing with the published data (Figure 8 in Jiang et al., 2022), we find a gap zone of fault slip (white area in the VW zone; $z = -4$ to -16 km in Figure 7 and $y = -30$ to 30 km in Figure 8) between the defined seismic and aseismic slip. Such a gap is not observed in the published data. The gap zone in Underworld means that the supposed seismic slip (defined by a threshold slip rate of 0.01 m/s) experienced slow slip at the VW zone (<0.01 m/s) before earthquake rupture initiates. We consider such slow slip events to be numerical artifacts since this gap is nearly filled when we adopt a shorter time step than the reference model (Figure 9). On the other hand, a model with a slightly longer time step than the reference model is also tested (Figure 10). The minimum time step used here is longer than 0.1 s (see the dashed line in Figure 10c) while that

Table 2
Codes Used in Comparison of BP5 Benchmark Model

Code name	Type	Simulation name	Reference
BICyclE	SBEM	Lambert	Lapusta and Liu (2009)
TriBIE	BEM	Li D.	Li and Liu (2016)
Unicycle	BEM	Barbot	Barbot (2021)
HBI	BEM	Ozawa	Ozawa et al. (2021)
ESAM	BEM	Liu Y.	Segall and Bradley (2012)
EQsimu	FEM	Liu D.	Liu et al. (2020)

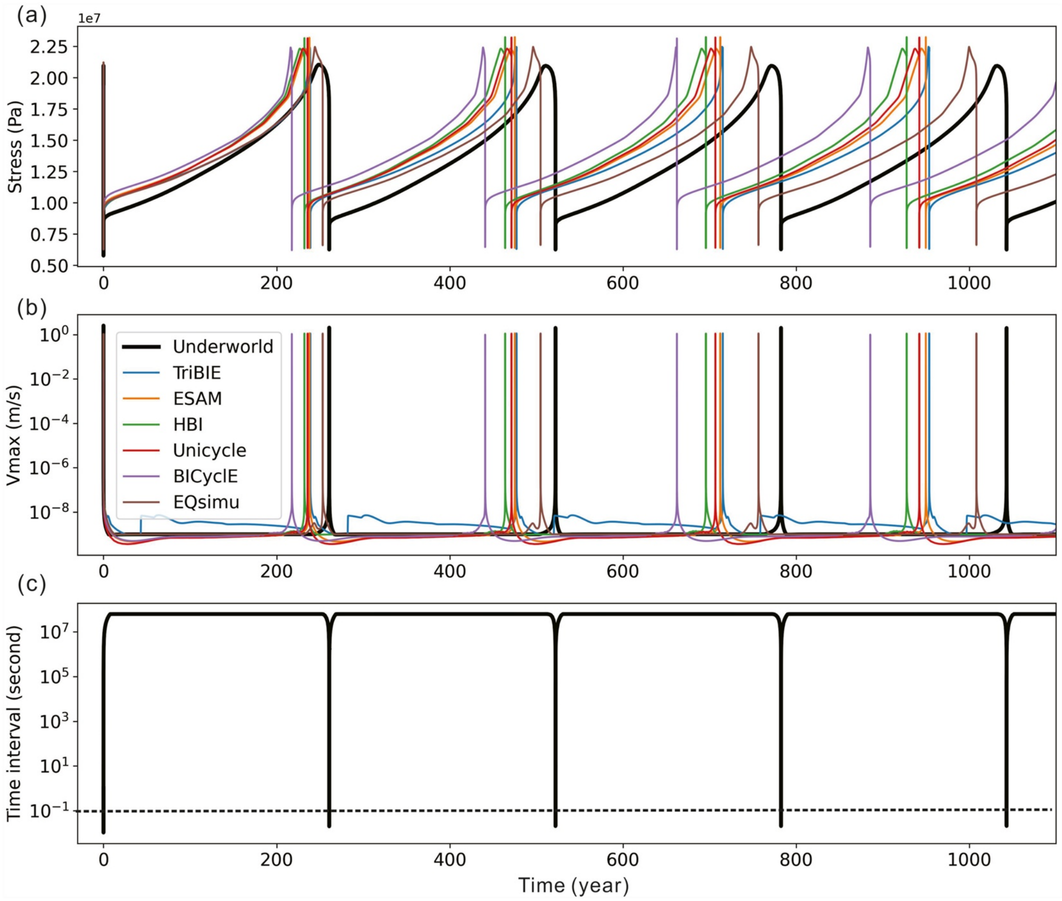

Figure 5. Evolution of the stress at the reference point (0, 0, −10 km) (a), maximum slip rate along the entire fault zone (b) and the adaptive time step used in simulation (c) for the reference model.

in the reference model is shorter than 0.1 s (see the dashed line in Figure 5c). With a longer timestep, the period of earthquake cycles is ∼230 years, almost the same as other modeling results. The shorter period of earthquakes than the reference model may be caused by lower stress drop after earthquakes, which results from the use of longer time steps. The extreme case is that if a time step longer than the Maxwell relaxation time is used, there would be no earthquake events and thus no stress drops in the viscoelastic media. Therefore, the choice of time step is very crucial to fault behavior, especially for the short-term dynamics. The stress change during an earthquake also affects the long-term earthquake cycles in numerical calculations.

In this benchmark, the vertical fault is conformed to one element, and the fault material is not mixed with wall rocks in any elements. We further test models with a fault of one and a half element width and do not find intensive stress fluctuations as is common for particle-in-cell methods when elements are filled with materials of high viscosity contrast (Yang, Moresi, & Mansour, 2021). We find that the stress field is also comparable with that of community models, but the maximum slip rate is almost twice of that from community models. This might be due to the calculation of fault slip rate by $2\dot{\varepsilon}_{\mathrm{II}} w_f$. Although the fault is designed to be of 1.5 element width, only central parts of the fault zone occupy one element, and both fault-wall rock interfaces are in elements containing two materials. Better ways to estimate the effective strain rate for the entire fault zone (Yang, Moresi, & Mansour, 2021) may address this issue but is beyond the topic of this study.

4. Case Study of Thrust Fault Earthquakes

4.1. Model Description

Thrust fault earthquakes happening on a non-planar fault plane are common in nature. It can be a bent subduction zone in inter-plate boundaries or an intraplate décollement fault. A two-dimensional (2D) crustal model (Figure 11a),

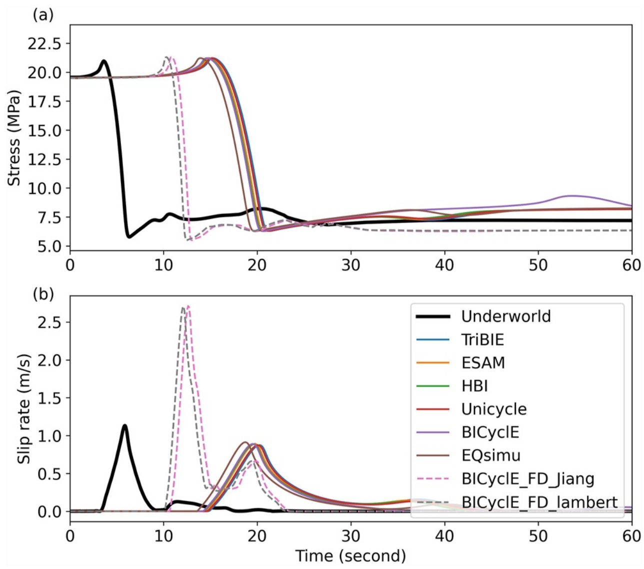

Figure 6. Stress (a) and slip rate (b) at the reference point (0, 0, −10 km) for the first 60 s since the initiation of the first event, which is defined with a threshold velocity of 0.1 m/s. The dashed line from BICyclE_FD_Jiang and BICyIE_FD_lambert (https://strike.scec.org/cvws/cgi-bin/seas.cgi) is based on fully dynamic simulations while other codes except Underworld are quasi-static simulations.

400-km long and 45-km wide, with a curved fault is designed to investigate the generic behaviors of earthquake cycles with 720 × 96 quadrilateral bilinear elements. The finite fault zone thickness is about six elements in size. Two cases of different cutting depths of the décollement fault are investigated. The fault geometry can be described by a parabolic equation, $z = (D_{top} - D_{base})/x_0^2(x - x_0)^2 + D_{top}$, where D_{base} (at $x = x_0$) and D_{top} (at $x = 0$ km) are the deepest and shallowest depths of the fault, respectively. One case has a D_{base} at a depth of 24 km while the other model has a D_{base} at a depth of 33 km, with $x_0 = -120$ km for both cases. They are, respectively, referred to as UP and LOW models based on the cutting depth. The VW zone extends from surface to a depth of 27 km, VS zone is from 30 km to the base at a depth 45 km and a transition zone of 3-km thickness is in between (Figure 11a). The entire fault in UP model is located within the VW zone in upper crust while LOW model cuts into the VS zone in lower crust. The fault zone has a distinctly low value of state variable (0.029 years) from wall rocks (1.9e16 years) to localize the deformation. Detailed parameters of this 2D model are listed in Table 3. A relatively high viscosity (10^{27} Pas) is applied to upper crust material, and the upper crust is supposed to be dominated by elastic deformation. The viscosity of the lower crust ranging from 10^{19} Pas to 10^{21} Pas is used to see how the strength of the lower crust affects earthquake cycles. This study focuses on the inter-seismic deformation of the free surface, which can be detected by geodetic observations. To make it easier to identify these models, we name different models after the cutting depth and lower crustal viscosity. For example, the UP model with a lower crust viscosity of 10^{21} Pas is named UP21. In addition, a 3D model is designed with the same fault geometry, frictional and rheological properties in x-z plane (-30 km $< y <$ 30 km) as the UP21 2D model to compare with 2D modeling results. The 3D model with a dimension of 240 × 96 × 45 km is simulated by 256 × 128 × 64 quadrilateral bilinear elements (Figure 11b).

4.2. Results

4.2.1. 2D Models

These models share some common evolution features, and we use the UP21 model as an example to illustrate generic patterns of earthquake cycles (Figure 12). The model is initially free of stress and the shear stress in upper crust linearly increases with a constant strain rate. The stress in upper crust is limited by the yielding stress of the

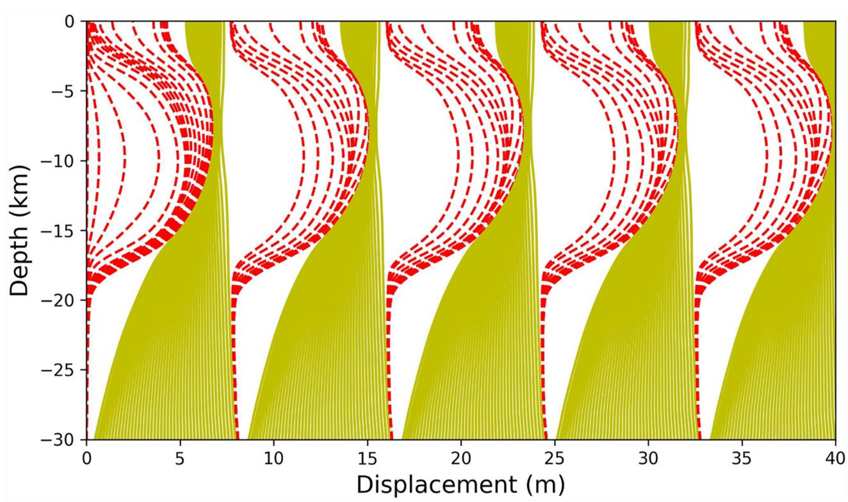

Figure 7. Cumulative fault slip evolution along a vertical profile ($y = 0$ km). The seismic slip (red lines) is plotted every 1 s and aseismic slip (yellow lines) is plotted every 5 years, with the threshold slip rate $V_{th} = 0.01$ m/s.

10.1029/2023GC010872

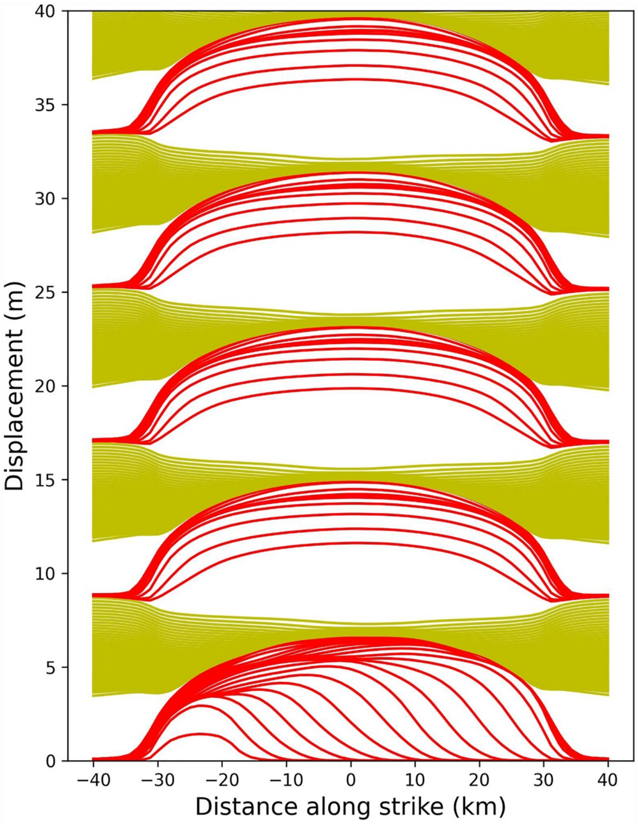

Figure 8. Cumulative fault slip evolution along a horizontal profile ($z = -10$ km). The seismic slip (red lines) is plotted every 1 s and aseismic slip (yellow lines) is plotted every 5 years, with the threshold slip rate $V_{th} = 0.01$ m/s.

rock, which is estimated to be 9 MPa with a constant normal stress of 30 MPa and a static frictional coefficient of 0.3. The stress in the lower crust is limited by the viscosity and strain rate. The first event happens after 10,000 years, which is longer than the characteristic relaxation time of lower crustal material (~1000 years). The lower crustal stress almost linearly increases in the first 1000 years, and then slows down with time. It approaches the upper limit of ~1.8 MPa, which approximates 2 $V/L\eta$, where $V = 1$ cm/year, $L = 400$ km and $\eta = 10^{21}$ Pas. After several (3–4) cycles, the stress evolves in a periodic way with a time interval between two sequential events of ~3800 years. The slip rate of the shallower reference point at a depth of 8 km crosses more than 8 orders of magnitude, with the co-seismic slip rate of ~0.1 m/s and inter-seismic slip rate $<10^{-9}$ m/s. Regarding the period of earthquake cycles for UP models, we find that the period decreases with lower crustal viscosity. The period for UP20 is ~3100 years and ~2100 years for UP19.

Figures 13 and 14 illustrates the influence of the lower crustal viscosity on inter-seismic movement of the free surface. In terms of Vx in both UP and LOW models, for the time no longer than a hundred years after one characteristic earthquake event, there are clear perturbations above the fault zone ($x = -100$ to 50 km) for models with lower crustal viscosity of 10^{19} Pas and 10^{20} Pas but not for higher crustal viscosity. After hundreds of years, there are almost no differences in Vx for models with different lower crustal strengths, and a linear trend occurs across the fault plane. In contrast, Vz in both UP and LOW models demonstrate clear signals related to fault movement, but the absolute magnitude at the same time after one earthquake event decays with the lower crustal viscosity. In LOW models, there is one major peak and one sub-peak. The major peak is located at $x = \sim -80$ km, the depth of which is the joint of the VW-VS transition zone and the fault plane. The sub-peak is located around $x = 0$ km, which is the fault trace on the surface. In LOW20 (Figure 14b), the sub-peak develops with time, while major peak decays with time. In the long run (time $> 7\tau$), the major peak at $x = -80$ km may disappear, and the sub-peak at $x = 0$ starts to dominate the deformation. In UP models, the two-peak patterns observed in LOW models are observable as well. In contrast to LOW models, the major peak (left one) appears not at

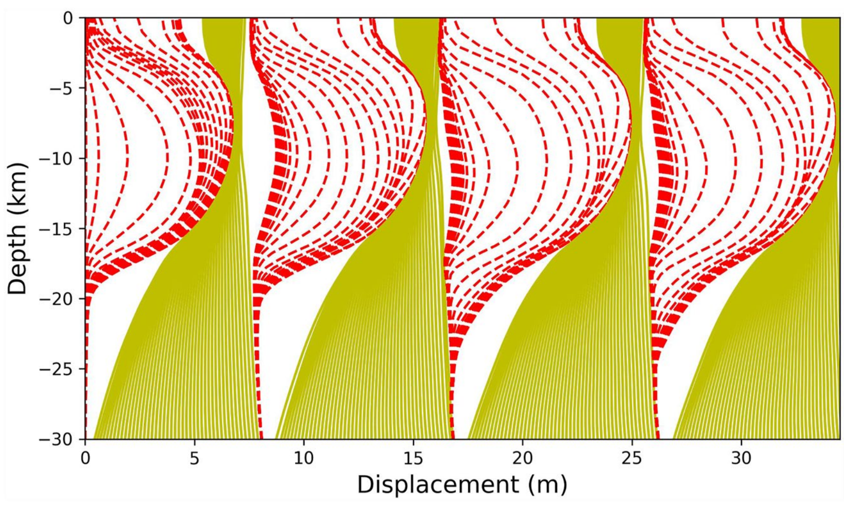

Figure 9. Cumulative fault slip evolution along a vertical profile ($y = 0$ km) with a shorter time step than the reference model. The seismic slip (red lines) is plotted every 1 s and aseismic slip (yellow lines) is plotted every 5 years, with the threshold slip rate $V_{th} = 0.01$ m/s.

10.1029/2023GC010872

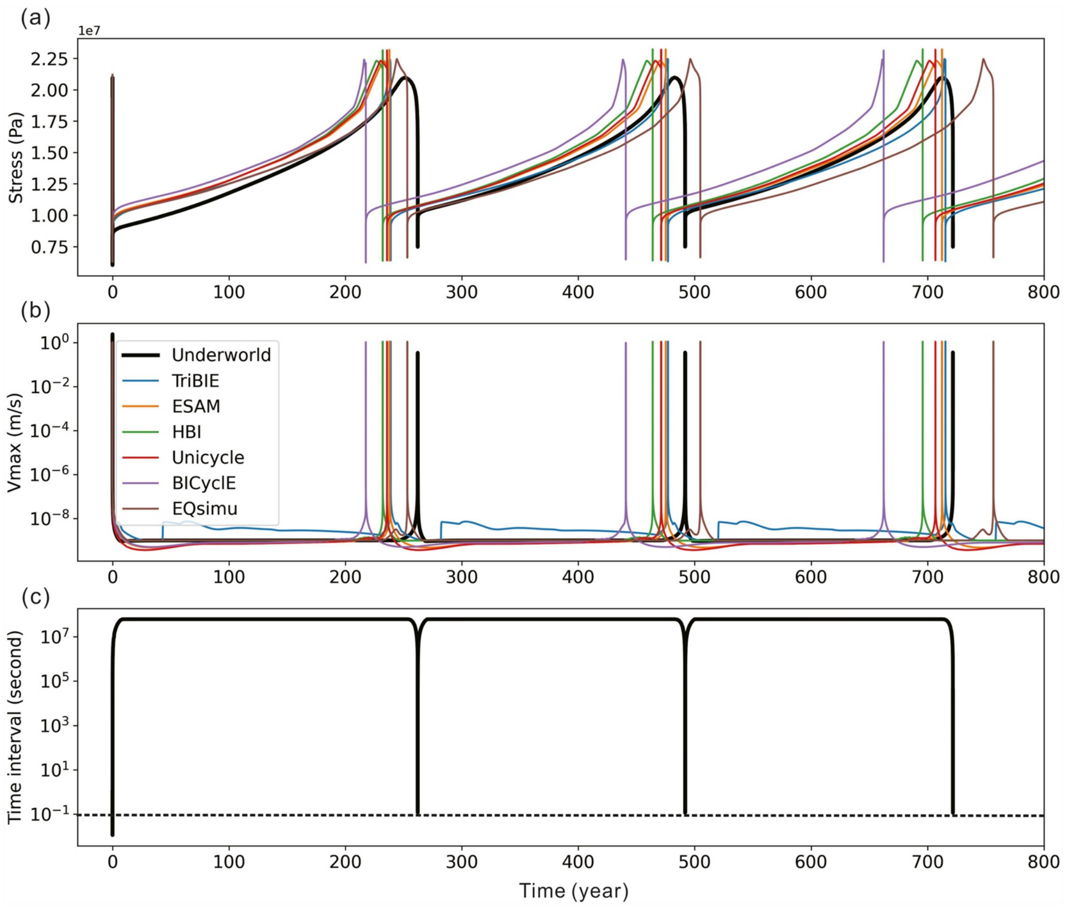

Figure 10. Evolution of the stress at the reference point (0, 0, −10 km) (a), maximum slip rate along the entire fault zone (b) and the adaptive time step used in simulation (c) for the model with longer time step than the reference model.

$x = -80$ km but shifts leftward to ∼120 km (except for the LOW19 model), corresponding to the leftmost tip of the fault zone. The sub-peak is located around $x = 0$ km as well. The major peak at $x = -120$ km decays with time as that in LOW models, but the sub-peak at $x = 0$ km almost does not change with time.

Peak patterns in model UP21 (Figure 13c) differ from other models in terms of the magnitude differences. For the time no longer than a hundred years after one characteristic earthquake event, the magnitude of sub-peaks is more than two thirds of the major peak. The sub-peaks in other models are generally less than half of the major peak.

4.2.2. 3D Models

The 3D model is designed to investigate how 2D modeling results can approximate 3D simulations. We focus on our study of the UP21 model with a fault cutting to a depth of 24 km and lower crustal viscosity of 10^{21} Pas. The map view of the top surface uplift rate also shows two peaks as what is observed in 2D models, one close to $x = 0$ km and the other one around $x = 100$ km (Figure 15). The magnitude of the peak above the fault down-dip end ($x = \sim 100$ km) is also higher than that at $x = 0$. In the fault strike direction (parallel to y direction), the right peak at $x = 0$ is limited by fault length (-30 km $< y <$ 30 km) while the position of the maximum uplift in the left peak at $x = \sim 100$ km extends beyond the fault length to the boundary plane of $y = \pm 48$ km. Note that this is caused by free-slip boundary condition along the $y = \pm 48$ km plane. Our further tests suggest that a zero slip of Vz in all vertical planes in the boundary limits the length of the left peak close to the fault length (-30 km $< y <$ 30 km) but is still longer and stronger than the right peak at $x = 0$ km.

Two profiles showing Vz at $y = 0$ km (solid line) and $y = -22.5$ km (dashed line) (Figure 16) have consistent patterns as the UP21 2D model in Figure 13c. The maximum value of the left peak at fault center ($y = 0$ km) is slightly (<0.005 cm/year) less than that in the quartile position ($y = -22.5$ km) while the maximum value of the

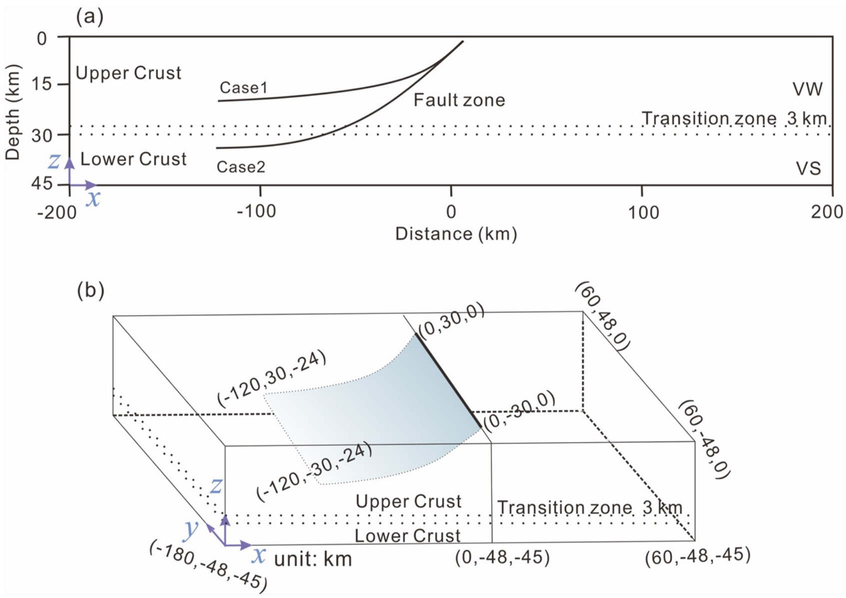

Figure 11. Setup of a two-dimensional (a) and three-dimensional (b) crustal model. (a) For the two-dimensional model, the right boundary is fixed, and the left boundary is applied with a constant velocity of 1 cm/year. Two cases of a fault zone, UP (case1) and LOW (case2), have distinct cutting depth in crust. (b) The three-dimensional model has the same fault geometry in x-z plane (-30 km $< y <$ 30 km) as the case1 in the two-dimensional model. The left boundary is applied with a constant velocity of 0.6 cm/year while the right boundary is fixed to have the same average inter-seismic strain rate in the locked fault zone. For both models, slip parallel to the boundary is free of stress.

right peak at fault center is slightly (<0.005 cm/year) higher than that in the quartile position. Comparing the absolute value of the peak in the 3D model with 2D models, we find that the maximum uplift rate (~0.135 cm/year at left peak) for the 3D model at ~10 years after one earthquake event is lower than that in the 2D model (0.18 cm/year) and is about three quarters of that in 2D models. This is caused by the assumption of an infinite long fault in 2D models, and the uplift rate of a 3D model is limited by finite fault length. Increasing fault length in 3D models tends to increase the uplift rate and is limited to results from 2D models.

4.3. Geodynamic and Seismic Hazard Indications

Different cases illustrated in Figure 11a may represent faults in different tectonic settings. The LOW models may represent mature faults cutting through the entire brittle upper crust into lower crust. The UP models may represent immature or shallow faults that are located within brittle upper crust. Any downward propagation of earthquake ruptures in LOW models may be stopped by VS zone due to high temperature in lower crust (Scholz, 1998) and the rupture propagation in UP models can be interrupted by high strength material or zones of low stress state near the down tip of the fault zone (Yang, Quigley, & King, 2021). In structure geology, fault zones in LOW models can be the dominant faults of a thick-skinned structure where the basement is involved in deformation (Rodgers, 1949), while UP models can be a thin-skinned structure where only surficial sedimentary rocks are deformed (Rodgers, 1949).

Table 3
Parameters in the 2D Thrust Fault Model

					RSF parameter					
	ρ (kg/m^3)	η (Pas)	G (Pa)	Depth (km)	a	b	D_{RS} (m)	μ^*_{st}	σ_n (MPa)	V_0 (m/s)
UC	2700	10^{27}	3e10	0–30	0.003	0.001[a]	0.01	0.3	30	4×10^{-9}
LC	2950	10^{19-21}	3e10	30–45	0.003	0.009	0.01	0.3	30	4×10^{-9}

[a]b linearly increases from 0.001 at 27 km to 0.009 at 30 km.

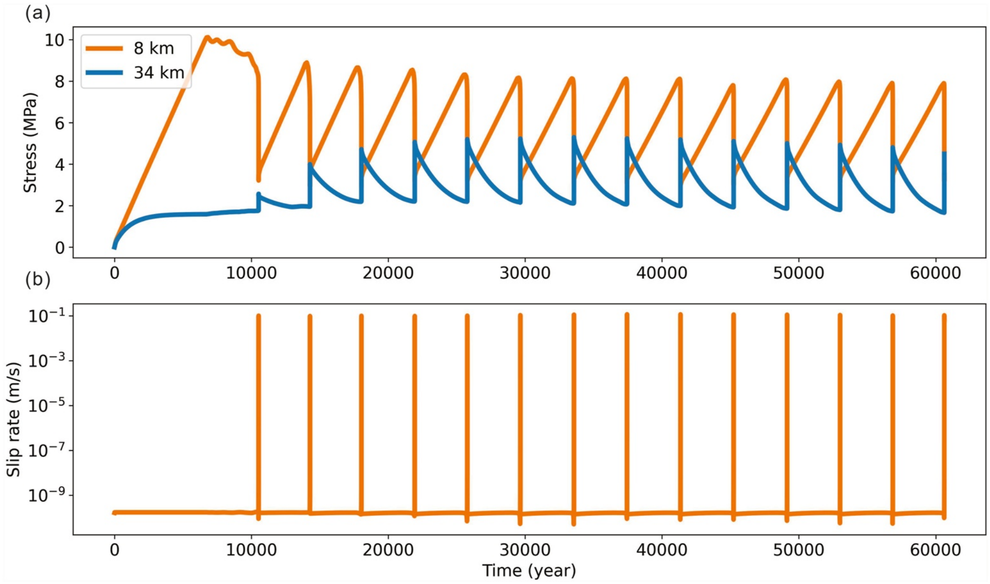

Figure 12. Evolution of the stress at the reference point at a depth of 8 km (orange) and 33 km (blue) in the fault zone (a) and slip rate (only for the shallow point) (b) for UP model with the lower crust viscosity of 10^{21} Pas, referred as model UP21.

Our models show that inter-seismic surface movement in both LOW and UP models is affected by lower crustal rheology. Generally, vertical uplift rate provides a more sensitive signal to lower crustal viscosity than horizontal slip rate. The major peak of the uplift rate profile after less than a hundred years corresponds to the lowermost point of the rupture in VW zone, which provides one way to estimate the potential rupture width for a characteristic earthquake. As the periodic time of earthquake cycles is also affected by lower crust viscosity, study areas with good constraints on frictional strength and normal stress on the fault plane, the periodic time of earthquake cycles can be used to infer the lower crustal viscosity. This provides an independent estimation of the lower crustal viscosity from conventional methods (Shi et al., 2015; M. Wang et al., 2021; Yang et al., 2020).

In terms of lower crustal viscosity estimation based on post-seismic relaxation, our study suggests that studies considering 2D profiles may overestimate lower crustal viscosity than 3D models (Hu et al., 2016; Zhu et al., 2022). To fit the same magnitude of uplift rate, 2D models require stronger lower crust in viscosity than 3D models. The 2D modeling results in Figures 13 and 14 suggest that decreasing the lower crustal viscosity by

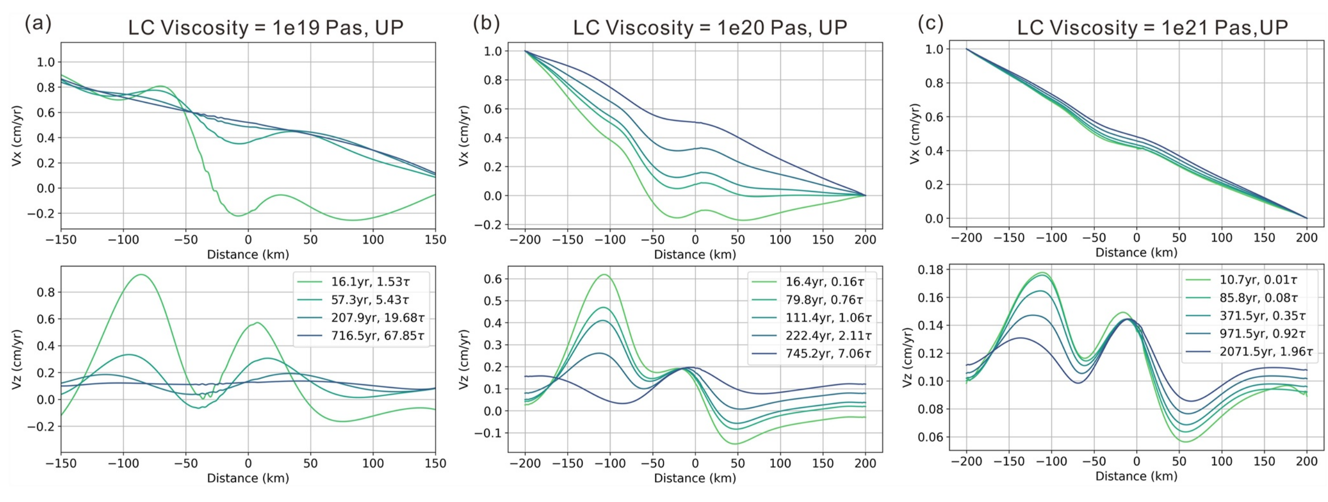

Figure 13. Horizontal (Vx) and vertical (Vz) post/inter-seismic movement at the top surface of the UP models. The lower crustal viscosity of 10^{19} Pas (a), 10^{20} Pas (b), and 10^{21} Pas (c) for each case illustrates how lower crustal viscosity affects post/inter-seismic deformations. The legend represents the absolute time (left column) and the time relative to the characteristic relaxation time τ (right column).

10.1029/2023GC010872

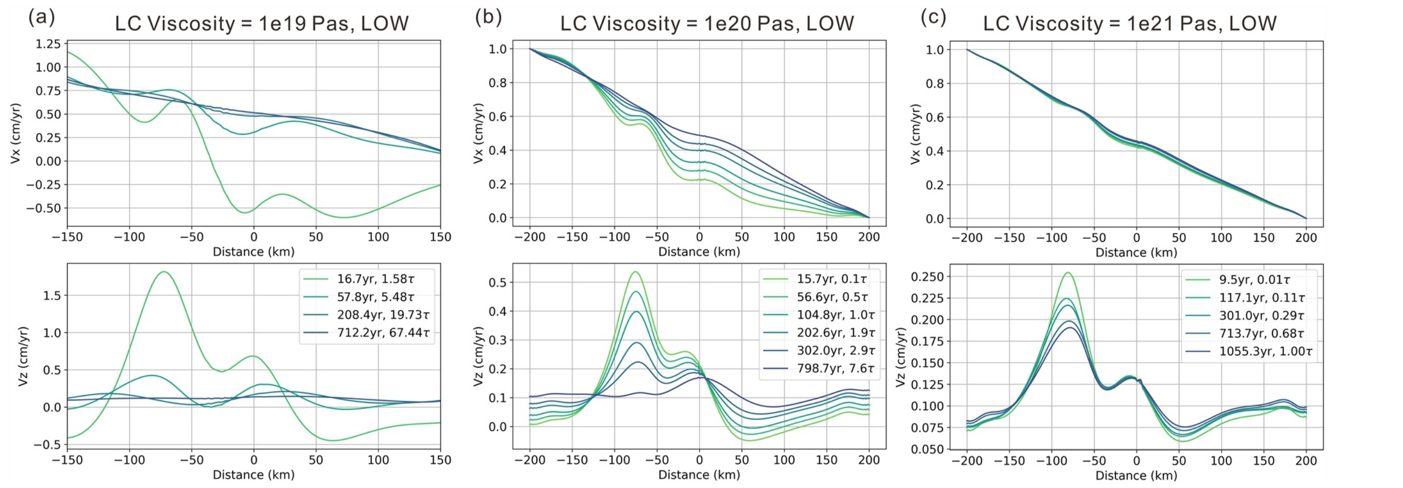

Figure 14. Horizontal (Vx) and vertical (Vz) post/inter-seismic movement at the top surface of the LOW models. The lower crustal viscosity of 10^{19} Pas (a), 10^{20} Pas (b), and 10^{21} Pas (c) for each case illustrates how lower crustal viscosity affects post/inter-seismic deformations. The legend represents the absolute time (left column) and the time relative to the characteristic relaxation time τ (right column).

one order of magnitude may increase the uplift rate by a factor of 2–3 times. Since the uplift rate in 3D models

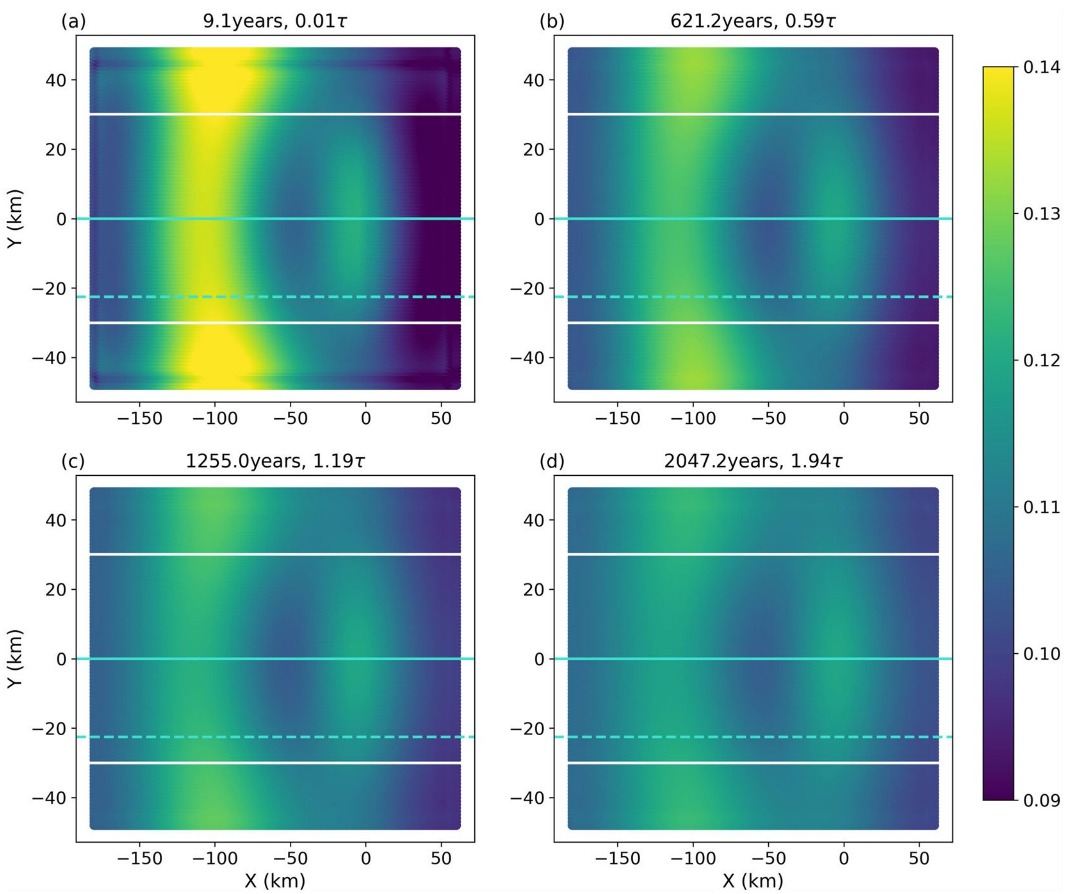

Figure 15. Surface uplift rate map of the three-dimensional model with a low crustal viscosity of 10^{21} Pas and a fault cutting to a depth of 24 km at 9.1 years (a), 621.2 years (b), 1255.0 years (c) and 2047.2 years (d) after one characteristic earthquake event. Two white lines at $y = \pm 30$ km mark two ends of the fault in y direction. The solid ($y = 0$ km) and dashed ($y = -22.5$ km) cyan lines are two profiles demonstrated in Figure 16. The unit of the map is cm/yr.

10.1029/2023GC010872

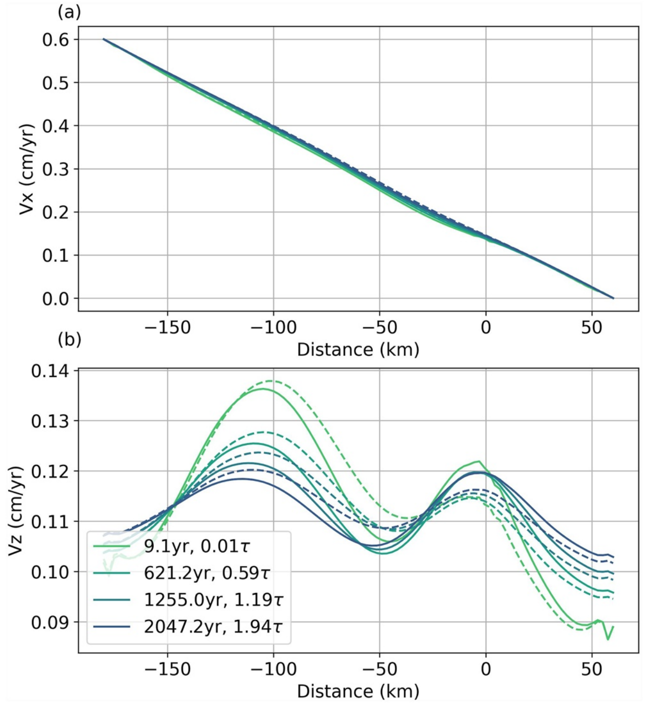

Figure 16. Horizontal (Vx) and vertical (Vz) post/inter-seismic movement at the top surface of the three-dimensional model for the profile at $y = 0$ km (solid line) and $y = -22.5$ km (dashed line).

is larger than half of that in 2D models, the overestimation of the lower crust should be less than one order of magnitude of the true value, which is generally within the uncertainty of the method (Hu et al., 2016; Zhu et al., 2022).

The model UP21 has a brittle upper crust of 30 km, viscosity in the lower crust of 1e21 Pas and the average strain rate in the crust is $\sim 10^{-16}$ 1/s. These settings are typical for stable cratons. Shallow earthquakes are also common in stable cratons. For example, earthquakes in cratonic continents in Australia and India are detected to be located less than 10 km deep below surface (Jackson & McKenzie, 2022; Yang, Quigley, & King, 2021). These so-called stable continents also produce destructive earthquakes (Yang, Quigley, & King, 2021); For example, the 1556 Huaxian earthquake (M 8.0), the deadliest earthquake in human history that killed 830,000 people, occurred in the middle of continental China. Seismic quiescent may in some cases relate to short instrumental histories (<~150 years) with respect to the earthquake cycles (>1000 years). For the characteristic earthquakes in stable continents, the model UP21 suggests that the Vx is not sensitive to fault activity at all, but the vertical displacements remain two peaks for more than 2000 years. The peak value in UP21 is >1 mm/year for both 2D and 3D models, that is still detectable for the state-of-the-art geodetic survey methods (Hao et al., 2014).

5. Conclusions

We build a code modeling earthquake cycle based on the Underworld software, which is designed for long-term large-scale tectonic simulations. The inertia term is first added, and the Navier-Stokes function is benchmarked against publications of viscous inertia flow modeling. Numerical solution calculated by Underworld for wave propagation in materials of Maxwell rheology is also compared with analytical solutions. These results suggest high mesh resolution and small time-step enable excellent agreements between Underworld solutions and other published numerical results or analytical solutions.

We further implement the RSF relationship for co-seismic fault slip in a visco-elastic-plastic model. A 3D earthquake cycle model is built to compare with results from the community code verification exercise for 3D dynamic modeling of sequences of earthquakes and aseismic slip. Although the Underworld code assumes incompressible material, it reproduces comparable periodic time of earthquake cycles, stress drop change after an earthquake event and co-seismic slip to the community code verification exercise. A relatively fast rupture propagation speed in Underworld may be attributed to Underworld considering fully dynamic rupture for incompressible material while others are quasi-dynamic modeling with compressible assumptions. The variable time stepping procedures are important in affecting transitions from aseismic (or slow slip) to seismic slip. It deserves further exploration in future work.

A curved thrust fault cutting to lower crust or located in brittle upper crust is investigated to see how lower crustal viscosity affects inter-seismic surface motion. Without changing the prescribed velocity boundary condition, increasing lower crustal viscosity tends to increase the periodic time of earthquake cycles and decrease the magnitude of the vertical motion rate. Two peaks are common in inter-seismic surface uplift profile across a reverse fault. The major peak, far from the fault trace, indicates the end point of the fault in the VW zone, and decays with time; the sub-peak is near the fault trace and almost remains unchanged. Shallow active faults in cratons with a strong lower crust are supposed to be detected by geodetic observations of uplift patterns around fault traces, where two peaks are of comparable magnitude.

Data Availability Statement

This study is based on published data, which are available as referenced in the article. The numerical open-source code Underworld2 version 2.10.0b (Mansour et al., 2020) is used for the calculations. The codes used in this study are available through GitHub (Yang & Giordani, 2023).

10.1029/2023GC010872

Acknowledgments
We first would like to thank Dr. Dave May and Dr. Junle Jiang for their constructive comments and suggestions, which are very helpful in improving our manuscript. The full dynamic results of the BP5 model are shared by Dr. Junle Jiang and Dr. Valere Lambert. This research was supported by National Natural Science Foundation of China (#42030306). Testing models are run with gadi in the National Computational Infrastructure (Canberra) and setonix in Pawsey (Perth).

References

Ampuero, J. P., & Ben-Zion, Y. (2008). Cracks, pulses and macroscopic asymmetry of dynamic rupture on a bimaterial interface with velocity-weakening friction. *Geophysical Journal International*, *173*(2), 674–692. https://doi.org/10.1111/j.1365-246x.2008.03736.x

Barbot, S. (2021). A spectral boundary-integral method for quasi-dynamic ruptures of multiple parallel faults. *Bulletin of the Seismological Society of America*, *111*(3), 1614–1630. https://doi.org/10.1785/0120210004

Ben-Zion, Y., & Rice, J. R. (1993). Earthquake failure sequences along a cellular fault zone in a three-dimensional elastic solid containing asperity and nonasperity regions. *Journal of Geophysical Research*, *98*(B8), 14109–14131. https://doi.org/10.1029/93jb01096

Biemiller, J., & Lavier, L. L. (2017). Earthquake supercycles as part of a spectrum of normal fault slip styles. *Journal of Geophysical Research: Solid Earth*, *122*(4), 3221–3240. https://doi.org/10.1002/2016jb013666

Brodsky, E. E., & van der Elst, N. J. (2014). The uses of dynamic earthquake triggering. *Annual Review of Earth and Planetary Sciences*, *42*(1), 317–339. https://doi.org/10.1146/annurev-earth-060313-054648

Burridge, R., & Knopoff, L. (1967). Model and theoretical seismicity. *Bulletin of the Seismological Society of America*, *57*(3), 341–371. https://doi.org/10.1785/bssa0570030341

Chen, T., & Lapusta, N. (2009). Scaling of small repeating earthquakes explained by interaction of seismic and aseismic slip in a rate and state fault model. *Journal of Geophysical Research*, *114*(B1), B01311. https://doi.org/10.1029/2008jb005749

Cochard, A., & Madariaga, R. (1994). Dynamic faulting under rate-dependent friction. *Pure and Applied Geophysics*, *142*(3–4), 419–445. https://doi.org/10.1007/bf00876049

Day, S. M., Dalguer, L. A., Lapusta, N., & Liu, Y. (2005). Comparison of finite difference and boundary integral solutions to three-dimensional spontaneous rupture. *Journal of Geophysical Research*, *110*(B12), B12307. https://doi.org/10.1029/2005jb003813

Dieterich, J. H. (1979). Modeling of rock friction: 1. Experimental results and constitutive equations. *Journal of Geophysical Research*, *84*(B5), 2161–2168. https://doi.org/10.1029/jb084ib05p02161

Dieterich, J. H. (1978). *Time-dependent friction and the mechanics of stick-slip, Rock friction and earthquake prediction* (pp. 790–806). Springer.

Durran, D. R. (1991). The third-order Adams-Bashforth method: An attractive alternative to leapfrog time differencing. *Monthly Weather Review*, *119*(3), 702–720. https://doi.org/10.1175/1520-0493(1991)119<0702:ttoabm>2.0.co;2

Farrington, R. J., Moresi, L. N., & Capitanio, F. A. (2014). The role of viscoelasticity in subducting plates. *Geochemistry, Geophysics, Geosystems*, *15*(11), 4291–4304. https://doi.org/10.1002/2014gc005507

Fey, U., König, M., & Eckelmann, H. (1998). A new Strouhal–Reynolds-number relationship for the circular cylinder in the range 47< Re< 2× 10 5. *Physics of Fluids*, *10*(7), 1547–1549. https://doi.org/10.1063/1.869675

Gerya, T. V. (2019). *Introduction to numerical geodynamic modelling*. Cambridge University Press.

Gerya, T. V., & Yuen, D. A. (2007). Robust characteristics method for modelling multiphase visco-elasto-plastic thermo-mechanical problems. *Physics of the Earth and Planetary Interiors*, *163*(1–4), 83–105. https://doi.org/10.1016/j.pepi.2007.04.015

Hao, M., Wang, Q., Shen, Z. K., Cui, D., Ji, L., Li, Y., & Qin, S. (2014). Present day crustal vertical movement inferred from precise leveling data in eastern margin of Tibetan Plateau. *Tectonophysics*, *632*, 281–292. https://doi.org/10.1016/j.tecto.2014.06.016

Harlow, F. H. (1964). The particle-in-cell computing method for fluid dynamics. *Methods in Computational Physics*, *3*, 319–343.

Herrendörfer, R., Gerya, T., & Van Dinther, Y. (2018). An invariant rate-and state-dependent friction formulation for viscoeastoplastic earthquake cycle simulations. *Journal of Geophysical Research: Solid Earth*, *123*(6), 5018–5051. https://doi.org/10.1029/2017jb015225

Hu, Y., Burgmann, R., Banerjee, P., Feng, L., Hill, E. M., Ito, T., et al. (2016). Asthenosphere rheology inferred from observations of the 2012 Indian Ocean earthquake. *Nature*, *538*(7625), 368–372. https://doi.org/10.1038/nature19787

Jackson, J., & McKenzie, D. (2022). The exfoliation of cratonic Australia in earthquakes. *Earth and Planetary Science Letters*, *578*, 117305. https://doi.org/10.1016/j.epsl.2021.117305

Jiang, J., Erickson, B. A., Lambert, V. R., Ampuero, J. P., Ando, R., Barbot, S. D., et al. (2022). Community-driven code comparisons for three-dimensional dynamic modeling of sequences of earthquakes and aseismic slip. *Journal of Geophysical Research: Solid Earth*, *127*(3), e2021JB023519. https://doi.org/10.1029/2021jb023519

Kolomenskiy, D., & Schneider, K. (2009). A Fourier spectral method for the Navier–Stokes equations with volume penalization for moving solid obstacles. *Journal of Computational Physics*, *228*(16), 5687–5709. https://doi.org/10.1016/j.jcp.2009.04.026

Lapusta, N., & Liu, Y. (2009). Three-dimensional boundary integral modeling of spontaneous earthquake sequences and aseismic slip. *Journal of Geophysical Research*, *114*(B9), B09303. https://doi.org/10.1029/2008jb005934

Lapusta, N., Rice, J. R., Ben-Zion, Y., & Zheng, G. (2000). Elastodynamic analysis for slow tectonic loading with spontaneous rupture episodes on faults with rate-and state-dependent friction. *Journal of Geophysical Research*, *105*(B10), 23765–23789. https://doi.org/10.1029/2000jb900250

Lee, E. H., & Kanter, I. (1953). Wave propagation in finite rods of viscoelastic material. *Journal of Applied Physics*, *24*(9), 1115–1122. https://doi.org/10.1063/1.1721458

Li, D., & Liu, Y. J. (2016). Spatiotemporal evolution of slow slip events in a nonplanar fault model for northern Cascadia subduction zone. *Journal of Geophysical Research: Solid Earth*, *121*(9), 6828–6845. https://doi.org/10.1002/2016jb012857

Liu, D., Duan, B., & Luo, B. (2020). EQsimu: A 3-D finite element dynamic earthquake simulator for multicycle dynamics of geometrically complex faults governed by rate-and state-dependent friction. *Geophysical Journal International*, *220*(1), 598–609. https://doi.org/10.1093/gji/ggz475

Mansour, J., Giordani, J., Moresi, L., Beucher, R., Kaluza, O., Velic, M., et al. (2020). Underworld2: Python geodynamics modelling for desktop, HPC and cloud [Software]. Zenodo. Journal of Open Source Software, *5*(47), 1797. https://doi.org/10.5281/zenodo.3975252

McKenzie, D. P. (1969). Speculations on the consequences and causes of plate motions*. *Geophysical Journal International*, *18*, 1–32. https://doi.org/10.1111/j.1365-246x.1969.tb00259.x

Moresi, L., Dufour, F., & Muhlhaus, H. B. (2002). Mantle convection modeling with viscoelastic/brittle lithosphere: Numerical methodology and plate tectonic modeling. *Pure and Applied Geophysics*, *159*(10), 2335–2356. https://doi.org/10.1007/s00024-002-8738-3

Moresi, L., Dufour, F., & Muhlhaus, H. B. (2003). A Lagrangian integration point finite element method for large deformation modeling of viscoelastic geomaterials. *Journal of Computational Physics*, *184*(2), 476–497. https://doi.org/10.1016/s0021-9991(02)00031-1

Moresi, L., Quenette, S., Lemiale, V., Meriaux, C., Appelbe, B., & Muhlhaus, H. B. (2007). Computational approaches to studying non-linear dynamics of the crust and mantle. *Physics of the Earth and Planetary Interiors*, *163*(1–4), 69–82. https://doi.org/10.1016/j.pepi.2007.06.009

Noda, H., & Shimamoto, T. (2010). A rate-and state-dependent ductile flow law of polycrystalline halite under large shear strain and implications for transition to brittle deformation. *Geophysical Research Letters*, *37*(9), L09310. https://doi.org/10.1029/2010gl042512

Ozawa, S., Ida, A., Hoshino, T., & Ando, R. (2021). Large-scale earthquake sequence simulations of 3D geometrically complex faults using the boundary element method accelerated by lattice H-matrices on distributed memory computer systems. arXiv preprint arXiv:.12165.

Palmer, A. C., & Rice, J. R. (1973). The growth of slip surfaces in the progressive failure of over-consolidated clay. *Proceedings of the Royal Society of London. A. Mathematical Physical Sciences*, *332*, 527–548.
Popov, A. A., & Sobolev, S. V. (2008). SLIM3D: A tool for three-dimensional thermomechanical modeling of lithospheric deformation with elasto-visco-plastic rheology. *Physics of the Earth and Planetary Interiors*, *171*(1–4), 55–75. https://doi.org/10.1016/j.pepi.2008.03.007
Rice, J. R. (1993). Spatio-temporal complexity of slip on a fault. *Journal of Geophysical Research*, *98*(B6), 9885–9907. https://doi.org/10.1029/93jb00191
Rice, J. R., & Ruina, A. L. (1983). Stability of steady frictional slipping. *Journal of Applied Mechanics*, *50*(2), 343–349. https://doi.org/10.1115/1.3167042
Rodgers, J. (1949). Evolution of thought on structure of middle and southern Appalachians. *AAPG Bulletin*, *33*, 1643–1654.
Rubin, A. M., & Ampuero, J. P. (2005). Earthquake nucleation on (aging) rate and state faults. *Journal of Geophysical Research*, *110*(B11), B11312. https://doi.org/10.1029/2005jb003686
Ruina, A. (1983). Slip instability and state variable friction laws. *Journal of Geophysical Research*, *88*(B12), 10359–10370. https://doi.org/10.1029/jb088ib12p10359
Scholz, C. H. (1998). Earthquakes and friction laws. *Nature*, *391*(6662), 37–42. https://doi.org/10.1038/34097
Segall, P., & Bradley, A. M. (2012). The role of thermal pressurization and dilatancy in controlling the rate of fault slip. *Journal of Applied Mechanics*, *79*(3), 031013. https://doi.org/10.1115/1.4005896
Shi, X. H., Kirby, E., Furlong, K. P., Meng, K., Robinson, R., & Wang, E. (2015). Crustal strength in central Tibet determined from Holocene shoreline deflection around Siling Co. *Earth and Planetary Science Letters*, *423*, 145–154. https://doi.org/10.1016/j.epsl.2015.05.002
Sleep, N. H. (1997). Application of a unified rate and state friction theory to the mechanics of fault zones with strain localization. *Journal of Geophysical Research*, *102*(B2), 2875–2895. https://doi.org/10.1029/96jb03410
Sobolev, S. V., & Muldashev, I. A. (2017). Modeling seismic cycles of great megathrust earthquakes across the scales with focus at postseismic phase. *Geochemistry, Geophysics, Geosystems*, *18*(12), 4387–4408. https://doi.org/10.1002/2017gc007230
Thomas, M. Y., Lapusta, N., Noda, H., & Avouac, J. P. (2014). Quasi-dynamic versus fully dynamic simulations of earthquakes and aseismic slip with and without enhanced coseismic weakening. *Journal of Geophysical Research: Solid Earth*, *119*(3), 1986–2004. https://doi.org/10.1002/2013jb010615
Tong, X., & Lavier, L. L. (2018). Simulation of slip transients and earthquakes in finite thickness shear zones with a plastic formulation. *Nature Communications*, *9*, 1–8. https://doi.org/10.1038/s41467-018-06390-z
Van Dinther, Y., Gerya, T. V., Dalguer, L. A., Corbi, F., Funiciello, F., & Mai, P. M. (2013). The seismic cycle at subduction thrusts: 2. Dynamic implications of geodynamic simulations validated with laboratory models. *Journal of Geophysical Research: Solid Earth*, *118*(4), 1502–1525. https://doi.org/10.1029/2012jb009479
Van Dinther, Y., Gerya, T. V., Dalguer, L. A., Mai, P. M., Morra, G., & Giardini, D. (2013). The seismic cycle at subduction thrusts: Insights from seismo-thermo-mechanical models. *Journal of Geophysical Research: Solid Earth*, *118*(12), 6183–6202. https://doi.org/10.1002/2013jb010380
Wang, K., Hu, Y., & He, J. H. (2012). Deformation cycles of subduction earthquakes in a viscoelastic Earth. *Nature*, *484*(7394), 327–332. https://doi.org/10.1038/nature11032
Wang, M., Shen, Z. K., Wang, Y., Bürgmann, R., Wang, F., Zhang, P. Z., et al. (2021). Postseismic deformation of the 2008 Wenchuan earthquake illuminates lithospheric rheological structure and dynamics of eastern Tibet. *Journal of Geophysical Research: Solid Earth*, *126*(9), e2021JB022399. https://doi.org/10.1029/2021jb022399
Williamson, C. H. K., & Brown, G. L. (1998). A series in $1/\sqrt{\mathrm{Re}}$ to represent the Strouhal–Reynolds number relationship of the cylinder wake. *Journal of Fluids and Structures*, *12*(8), 1073–1085. https://doi.org/10.1006/jfls.1998.0184
Yang, H., & Giordani, J. (2023). underworld-community/uw-earthquake-cycles: v1.0 (Version 1.1.0). [Software]. Zenodo. https://doi.org/10.5281/zenodo.8251145
Yang, H., Moresi, L. N., & Mansour, J. (2021). Stress recovery for the particle-in-cell finite element method. *Physics of the Earth and Planetary Interiors*, *311*, 106637. https://doi.org/10.1016/j.pepi.2020.106637
Yang, H., Moresi, L. N., & Quigley, M. (2020). Fault spacing in continental strike-slip shear zones. *Earth and Planetary Science Letters*, *530*, 115906. https://doi.org/10.1016/j.epsl.2019.115906
Yang, H., Quigley, M., & King, T. R. (2021). Surface slip distributions and geometric complexity of intraplate reverse-faulting earthquakes. *GSA Bulletin*, *133*(9–10), 1909–1929. https://doi.org/10.1130/b35809.1
Zhu, Y. G., Diao, F. Q., Wang, R. J., Hao, M., Shao, Z. G., & Xiong, X. (2022). Crustal shortening and rheological behavior across the Longmen Shan Fault, Eastern Margin of the Tibetan Plateau. *Geophysical Research Letters*, *49*(11), e2022GL098814. https://doi.org/10.1029/2022gl098814